

Compare Results

Old File:

egosphere-2023-633-manuscript-version4.pdf

38 pages (29.33 MB)

10/16/2023 3:15:12 PM

versus

New File:

HiDRON_Paper__Fourth_revision.pdf

38 pages (29.77 MB)

3/21/2024 12:25:04 AM

Total Changes

1099

Content

312 Replacements

299 Insertions

269 Deletions

Styling and Annotations

41 Styling

178 Annotations

[Go to First Change \(page 1\)](#)

High-altitude atmospheric turbulence and infrasound measurements using a balloon-launched small uncrewed aircraft system

Anisa N. Haghghi¹, Ryan D. Nolin¹, Gary D. Pundsack², Nick Craine², Aliaksei Stratsilatau³, and Sean C. C. Bailey¹

¹Department of Mechanical and Aerospace Engineering, University of Kentucky, Lexington, Kentucky 40506, USA

²Stratodynamics Inc., 16192 Coastal Highway, Lewes, Delaware 19958, USA

³UAVOS Inc., 541 Jefferson Ave, Ste 100, Redwood City, California 94063, USA

Correspondence: Sean Bailey (sean.bailey@uky.edu)

Abstract. This study investigates the use of a balloon-launched Uncrewed Aircraft System (UAS) for the measurement of turbulence in the troposphere and lower stratosphere. The UAS was a glider which could conduct an automated descent following a designated flight trajectory and was equipped with in-situ sensors for measuring thermodynamic and kinematic atmospheric properties. In addition, this aircraft was equipped with an infrasonic microphone to assess its suitability for the remote detection of clear-air turbulence. The capabilities of the UAS and sensing systems were tested during three flights conducted in 2021 in New Mexico, U.S.A.. It was found that the profiles of temperature, humidity and horizontal winds measured during descent were in broad agreement with those made by radiosonde data published by the U.S. National Weather Service, separated by up to 380 km spatially and by 3 to 5 hours temporally. Winds measured during controlled flight descent were consistent with the winds measured by global-positioning-system-derived velocity during balloon ascent. During controlled descent with this particular payload, nominal vertical resolution on the order of 1 m during was achieved for temperature, relative humidity and pressure with a nominal vertical resolution of wind velocity vector on the order of 0.1 m, with the aircraft having a glide slope angle from 1° to 4°. Analysis approaches were developed that provided turbulent kinetic energy and dissipation rate, but it was found that the corresponding Richardson number was sensitive to the methodology used to determine the vertical gradients from a single flight. The low-frequency response of the infrasonic microphone was found to correlate to long wavelength wind velocity fluctuations measured at high altitude, and broadband response measured within boundary layer turbulence.

Copyright statement. Author(s) 2024. This work is distributed under the Creative Commons Attribution 4.0 License.

1 Introduction

By enhancing the exchange of mass, momentum, and energy, the formation and evolution of atmospheric turbulence provides a significant contribution to weather and climate. As atmospheric turbulence is expected to increase in frequency and intensity in response to climate change (e.g. Williams and Joshi, 2013), increased understanding of its role in atmospheric dynamics

is needed. The presence of atmospheric turbulence, particularly clear air turbulence, also poses an aviation hazard that is challenging to predict and detect. This latter point is particularly true for high-altitude autonomous flight, a regime which is being increasingly pursued in the form of High-Altitude Pseudo-Satellite aircraft intended to provide communication and remote observation capabilities at relatively low cost (Gonzalo et al., 2018; D'Oliveira et al., 2016; Hasan et al., 2022). By the nature of the low density conditions under which these aircraft are designed to operate, they tend to be lightweight with narrow performance envelopes for which controlled flight can be maintained, making them susceptible to atmospheric disturbances. Hence, there is motivation to improve our ability to measure and predict stratospheric and high altitude turbulence, which can occur due to shear instabilities or gravity wave breaking despite the higher static stability at these altitudes. Turbulence in the upper troposphere may also be introduced through mesoscale convective systems (Liu et al., 2014), mountain waves (Cunningham and Keyser, 2015) and wind shear (e.g. as introduced by the jet stream).

Although the turbulence intensity is commonly quantified through the turbulent kinetic energy per unit mass

$$k = \frac{1}{2} \overline{u'_i u'_i}, \quad (1)$$

atmospheric turbulence is often also characterized through the related turbulent kinetic energy dissipation rate, formally defined as

$$\varepsilon = \frac{1}{2} \nu \overline{\left(\frac{\partial u'_i}{\partial x_j} + \frac{\partial u'_j}{\partial x_i} \right)^2}. \quad (2)$$

Here, summation notation has been used with the index indicating the wind velocity components, u_i , and direction components x_i . Furthermore, ν indicates the kinematic viscosity, and $u'_i = u_i - \overline{u_i}$ indicates the unsteady contribution to the velocity component, with the overline denoting an average value.

The presence of turbulence is often related to the local gradient Richardson number

$$Ri = \frac{g}{\theta_v} \frac{\partial \overline{\theta_v}}{\partial x_3} \left(\frac{\partial u_1}{\partial x_3} \right)^2 + \left(\frac{\partial u_2}{\partial x_3} \right)^2 \quad (3)$$

where g is the gravitational acceleration,

$$\theta_v = T \left(\frac{100000}{P} \right)^{0.2861} (1 + 0.61q) \quad (4)$$

is the virtual potential temperature, u_1 and u_2 are the horizontal components of the wind velocity vector, x_3 is the spatial component aligned in the direction opposing g , q is the water vapor mixing ratio, T is the temperature in Kelvin and P is the pressure in Pascals. The static stability is quantified through the square Brunt-Väisälä frequency,

$$N^2 = \frac{g}{\theta_v} \frac{\partial \overline{\theta_v}}{\partial x_3} \quad (5)$$

and the square shear frequency provides a measure of potential for turbulence production due to mean velocity shear

$$S^2 = \left(\frac{\partial \bar{u}_1}{\partial x_3} \right)^2 + \left(\frac{\partial \bar{u}_2}{\partial x_3} \right)^2. \quad (6)$$

Hence, $Ri = N^2/S^2$, can also be used to attribute the source of turbulence as being from convective or shear instabilities (Söder et al., 2021; Sharman et al., 2014; Kim et al., 2020), and introduces the potential to model the relationship between turbulence in the stratosphere and tropospheric activity (Chunchuzov et al., 2021). A critical Richardson number of $Ri = 0.25$ (below which turbulence is likely) has been empirically identified, although a range of critical values $0.25 < Ri < 1$ have also been proposed (Abarbanel et al., 1984; Galperin et al., 2007).

When considering stratospheric turbulence measurements, most experiments have been conducted using balloon-borne instruments (e.g. Wescott et al., 1964; Ehrenberger, 1992; Haack et al., 2014; Alisse et al., 2000; Gavrilov et al., 2005) with some of the earliest of these experiments conducted in the 1960s (Enlich and Mancuso, 1968). Among the most relevant conclusions from these studies is that stratospheric turbulence tends to form in relatively thin atmospheric layers due to intrinsic static stability at these altitudes. In many cases, meteorological balloon soundings rely on indirect measures of turbulence, for example through application of the analysis proposed by Thorpe and Deacon (1977) which analyzes temperature profiles to infer ε and the Thorpe length scale (e.g. Clayson and Kantha, 2008).

One series of balloon-borne experiments investigating stratospheric turbulence using direct measures was the Leibniz-Institute Turbulence Observations in the Stratosphere (LITOS) experiments. The experiments, conducted by LITOS (Haack et al., 2014), were conducted using balloons equipped with a thermal anemometer to measure velocity and temperature fluctuations at high frequency. The resulting measurements were within sub-centimeter resolution, and therefore suitable for resolving the finer scales of turbulence. This experiment reached altitudes up to 30 km, and when ε was compared to both Ri and an increase in ε with altitude was observed with clear correlation between turbulent events and $Ri < 0.25$ (Haack et al., 2014). However, in some instances turbulent events were also observed when $Ri > 0.25$ although other studies attribute such behavior to the specifics of the Ri calculation (Galperin et al., 2007; Haack et al., 2014) and later studies suggest that the measurements may have been contaminated by the balloon wake (Söder et al., 2019).

Remote sensing techniques have also been deployed for turbulence studies, for example through the use of radar to measure the turbulent kinetic energy dissipation rate (Bertin et al., 1997; Fukao et al., 1994; Sato and Woodman, 1982; Barat and Bertin, 1984). Early studies found radar-determined dissipation rates were often underestimated due to the low vertical resolution. However, very-high-frequency and ultra-high-frequency radar measurements have presented a better prospect to resolve thin layers of clear air turbulence (Barat and Bertin, 1984). For example, an altitude resolution of 150 m was able to detect the thin layers of turbulence in the lower stratosphere (Sato and Woodman, 1982).

Crewed aircraft measurements have also been utilized to measure high altitude turbulence (e.g. Nastrom and Gage, 1985). Currently, routine measurements of atmospheric turbulence are conducted for operational forecasting through Aircraft Meteorological Data Relay (AMDAR) reports generated by in-situ measurement systems on commercial aircraft using a turbulence detection algorithm developed by Sharman et al. (2014). These systems generally report the turbulence intensity in the form of

80 eddy dissipation rate (*EDR*), defined as

$$EDR = \varepsilon^{1/3}, \tag{7}$$

✘ which is currently used as a standard for turbulence reporting by the International Civil Aviation Organization. In the AMDAR *EDR* calculation, a fully-formed von Kármán inertial subrange is assumed, and the *EDR* is determined from either vertical-wind measurements, or the aircraft's gust response measured through acceleration.

85 Recently, it has become increasingly common to use uncrewed aircraft, or uncrewed aerial systems (UAS), equipped with in-situ sensors (e.g. hot-wire anemometers, sonic anemometers, hot-film probes, pitot tubes, or multi-hole pressure probes) for studies of turbulence in the atmospheric boundary layer and troposphere (e.g. Egger et al., 2002; Hobbs et al., 2002; Balsley et al., 2013; Witte et al., 2017; Rautenberg et al., 2018; Bärfuss et al., 2018; Jacob et al., 2018; Bailey et al., 2019; Al-Ghussain and Bailey, 2022; Lawrence and Balsley, 2013; ✘ Balsley et al., 2018; Reuder et al., 2012; Calmer et al., 2018; Luce et al., 2020; 90 Kantha et al., 2017). Many of the UAS used for turbulence studies employ multi-hole probes, which measure the dynamic pressure of the air, with multiple pressure ports combined with a directional calibration used to determine the wind vector components relative to the probe axis. Due to their fragility, hot-wire probes, which measure the convective heat transfer across a very thin heated filament, are usually reserved for short-term scientific studies although they are standard instruments on some UAS (e.g. Hamilton et al., 2022). The fast response of the ✘ hot-wire anemometer allows detailed characterization of the 95 turbulence, for example by allowing the measurement of small-scale fluctuations.

An additional sensing approach which has the potential to measure turbulence is the detection of infrasound (✘ Shams et al., ✘ ✘ ✘ 2013), i.e. acoustic frequencies below 20 Hz. This can be done through application of infrasonic microphones typically used for seismic detection and marine acoustics. Within the atmospheric boundary layer, the infrasound energy from ground-based arrays has been found to correspond to the turbulent kinetic energy in the atmosphere, particularly when buoyantly-produced 100 convective turbulence is present (Cuxart et al., 2015). The infrasound energy levels were also found to increase in the presence of elevated jets or turbulence above the measurement height, which was thought to be caused by the sound generated at higher altitudes reaching the microphones. In balloon-borne measurements, it has been found that it is possible to detect acoustic low frequency signals, such as microbaroms, using sensitive infrasonic sensors (Bowman and Lees, 2015). The advantage of ✘ infrasonic sensors for turbulence detection is that acoustic propagation increases at low frequency and low kinematic viscosity 105 (Whitaker and Norris, 2008) which allows propagation over distances ranging between a few hundred to a few thousand of kilometers. For example, an array of ground-based microphones were able to detect clear air turbulence at distances up to 360 km (Shams et al., 2013).

Here, we present measurements from a balloon-launched stratospheric glider UAS intended for turbulence measurement. These flights were conducted with the aircraft equipped both with standard in-situ sensors as well as a novel infrasonic micro- 110 phone in order to test the potential of using airborne acoustic signatures to remotely detect the presence of turbulence. This configuration was tested in a series of three high-altitude flight tests with the aircraft carried by balloon from 25 km up to 30 km above sea level. After reaching these altitudes, it was released from the balloon and conducted autonomous flight to a desig-

nated measurement location, thereafter following a pre-programmed helical flight path to a designated landing location. During its descent, the aircraft's glide slope was 1° to 4° , which allowed it to measure a wide range of turbulence scales horizontally at high vertical resolution, while maintaining a relatively constant location over the surface. One drawback of this approach is that the current regulatory environment means deploying this type of UAS within a national airspace system requires permission from the corresponding regulatory body, requiring additional measures to ensure deconfliction with crewed aircraft. Here, the flights were conducted in the restricted airspace above Spaceport America, New Mexico U.S.A., coordinating with the adjacent White Sands Missile Range and utilizing airspace closed to crewed aircraft. However, this approach to deconfliction restricts the geographical location at which such measurements can be taken.

The remainder of this manuscript is divided into three main sections: Section 2 describes the aircraft and measurement systems, along with information about the flight location and flight path; Section 3 describes the approaches which were used to extract turbulence statistics from the data acquired during the flights; with Section 4 summarizing the main findings from this study.

2 Experiment Description

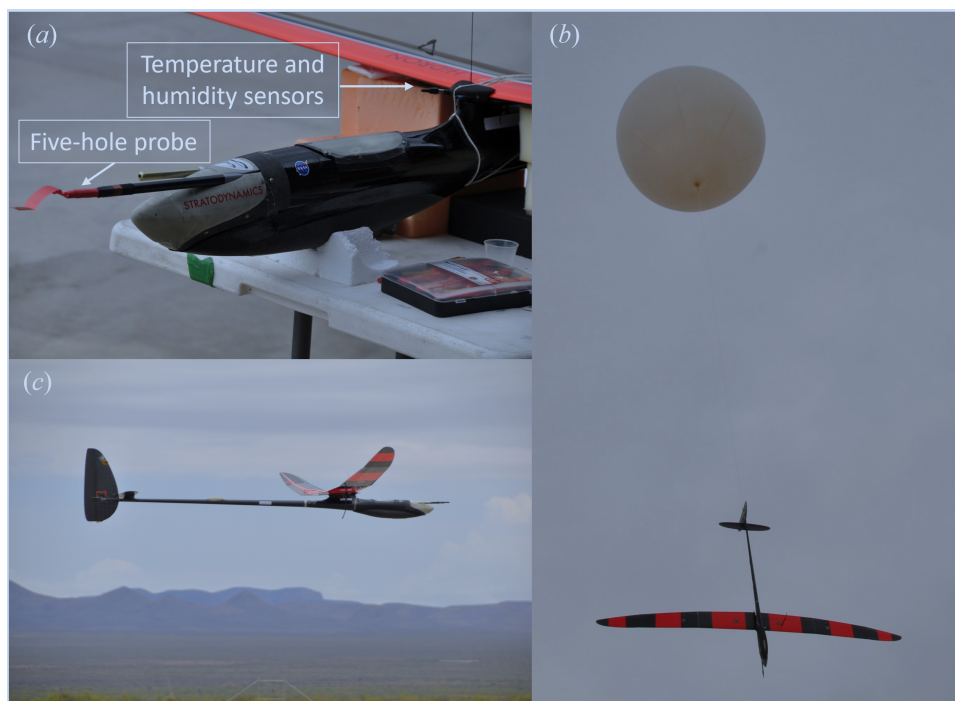


Figure 1. Images of HiDRON H2 showing: (a) close up of aircraft nose showing five-hole probe and temperature and humidity sensor location; (b) aircraft during launch; and (c) aircraft during landing.

2.1 Aircraft

Key to this research was the use of the host UAS platform, the HiDRON H2 (see Fig. 1), operated by Stratodynamics Inc. The HiDRON H2 is a balloon-launched carbon-fiber/fiberglass glider UAS that is capable of autonomous and soaring flight modes. It has a wingspan of 3.8 m and its nominal flight weight is approximately 5.7 kg with the payload. To achieve initial altitudes in excess of 30 km, the HiDRON H2 is launched using latex sounding balloons. Different sizes of balloons were used in this study with 2000 g, 1200 g and 3000 g balloons employed for each of three flights, referred to as Flights 1, 2 and 3, respectively. After release, the aircraft is controlled by a UAVOS Inc. autopilot to follow a pre-programmed descent pattern towards a designated landing point. An operator can track the HiDRON H2 position from launch to landing and changes to the flight plan can be made in real time through radio telemetry, which also allows operational parameters to be transmitted to the ground at distances up to 100 km. Full telemetry information was produced at 10 Hz by the autopilot for all three flights, including location, ground speed, 6 degree-of-freedom orientation information as well as pressure, temperature and humidity information from an integrated sensing system. This 10 Hz sample rate telemetry was intrinsic to the radio modem used for the command-and-control link and telemetry. The specific rate was selected for maximum efficiency in the transmission and recording of data packets and to maintain reliability of the radio communication and corresponding command-and-control link.

Other safety features include a parachute, dual-redundant balloon release system and geofencing safety protocols that prevent the aircraft from leaving the designated airspace. During prior flights, including flights exceeding altitudes of 30 km, the HiDRON H2 has shown reliability in remaining controllable in high-wind (as high as 32 m s^{-1}), operating in low-temperature conditions ($< -60^\circ\text{C}$), and in returning to a predefined landing site. For the flights reported here, the winds were less than 25 m s^{-1} and the minimum temperature was -65°C .

For all flights, the autopilot was set to maintain the aircraft's kinetic energy (reflected through the indicated airspeed), with the value selected near the optimal lift-to-drag ratio (the maximum distance that can be travelled per loss in altitude). To maintain the set airspeed the autopilot adjusts the pitch angle on the elevator to control the angle of attack of the main wing airfoil. The velocity of the aircraft relative to the air, \mathbf{V}_R , may therefore fluctuate slightly due to the pitch angle adjustments. Also, as the aircraft descends in altitude the air density increases and the HiDRON H2's aerodynamic performance improves; thus, \mathbf{V}_R gradually decreased as the aircraft descended. Figure 2 shows the magnitude of horizontal ground speed, $|\mathbf{V}_G|$, descent speed, V_D , relative to the ground, as well as the magnitude of the aircraft's velocity relative to the air, $|\mathbf{V}_R|$, for the helical descent portion of each of the three flights as a function of the altitude above sea level (a.s.l.). The horizontal velocities are related through $\mathbf{V}_R = (V_{G_x} - u)\mathbf{e}_1 + (V_{G_y} - v)\mathbf{e}_2 - (V_D e + w)\mathbf{e}_3$ where $\mathbf{V}_G = V_{G_x}\mathbf{e}_1 + V_{G_y}\mathbf{e}_2$ is the horizontal velocity of the aircraft relative to the ground in the Earth-fixed, inertial frame of reference with $\mathbf{e}_1, \mathbf{e}_2, \mathbf{e}_3$ the basis vectors aligned to the East, North, and up, respectively. The vector $\mathbf{U} = u\mathbf{e}_1 + v\mathbf{e}_2 + w\mathbf{e}_3$ is the wind vector and $-V_D\mathbf{e}_3$ the aircraft's descent speed in the inertial frame. The method used to obtain the wind velocity vector is provided in Section 2.2.

As noted above, to measure atmospheric conditions, the aircraft was equipped with an integrated InterMet Systems iMet-XF atmospheric sensing system having fast-response bead thermistor to measure air temperature, T , and a capacitive relative humidity, RH , sensor. The manufacturer-provided specifications (International Met Systems) state the pressure sensor provided

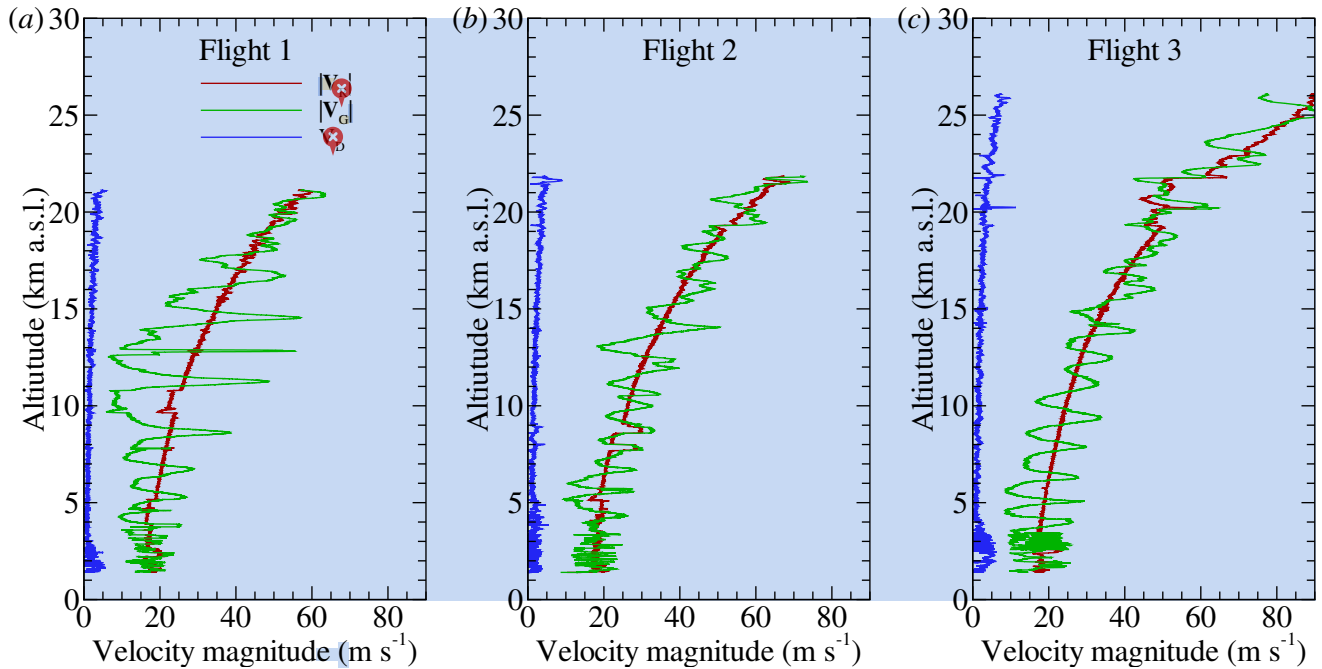


Figure 2. Horizontal ground speed in inertial Earth-fixed coordinates, $|V_G|$, magnitude of the descent speed in inertial Earth-fixed coordinates, V_D , and relative air velocity magnitude in aircraft-fixed coordinates, $|V_R|$, for (a) Flight 1, (b) Flight 2 and (c) Flight 3.

160 a ± 1.5 hPa accuracy for pressure, P , with humidity sensor supporting a full 0 - 100 %RH range at ± 5 %RH accuracy with a
 165 resolution of 0.7 %RH. The temperature sensor provided a $\pm 0.3^\circ\text{C}$ accuracy with a resolution of 0.01°C up to a maximum of
 50°C. The stated response times of these sensors are on the order of 10 ms for pressure, 5 s for humidity and 2 s for temperature
 in still air, with the autopilot sampling these sensors at 10 Hz. The pressure and temperature sensors were mounted with the
 sensing elements exposed to the airflow upstream of the wing support (see Fig. 1a) to ensure aspiration of the sensors during
 forward flight.

2.2 Payload

The turbulence-measuring payload was a combination of four components: (1) a five-hole probe; (2) an infrasonic microphone;
 (3) a data acquisition board; and (4) an embedded computer. These components were installed in the nose of the HiDRON H2,
 which could be accessed via removal of the nose cone, as shown in Fig. 3c.

170 2.2.1 Five-Hole Probe:

Wind speed and direction relative to the aircraft were measured using a bespoke five-hole probe mounted such that the probe
 projected upstream of the nose of the aircraft, as shown in Fig. 1. The probe, detailed in Fig. 3a, is similar to that used in Bailey
 et al. (2019, 2020); Al-Ghussain and Bailey (2022) and was manufactured from a carbon-fiber tube equipped with a beveled

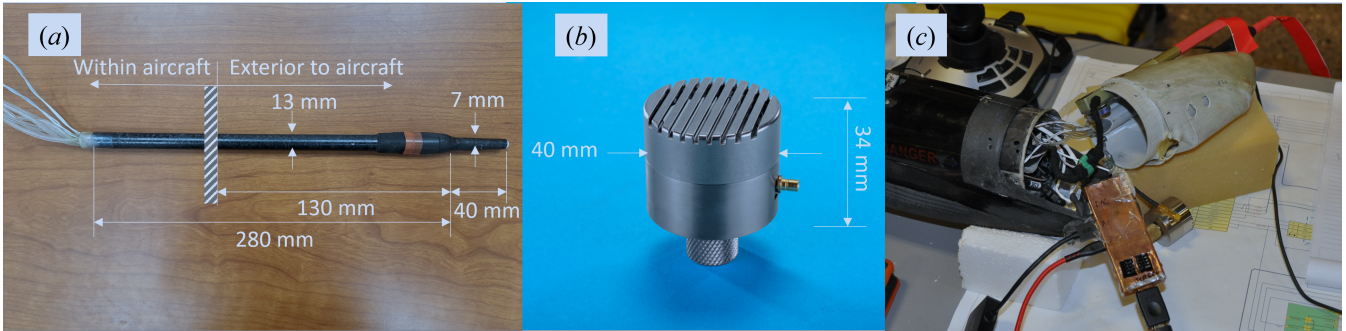


Figure 3. (a) Five-hole probe, (b) infrasonic microphone, and (c) nose payload bay open between flights, with embedded computer shown removed for data retrieval. Infrasonic microphone is below embedded computer but was installed in aircraft nose facing forward during flight.

aluminum tip. The tip of the probe was arranged with one center hole normal to the probe axis surrounded by four other holes arranged symmetrically around it having their plane normal vector aligned 20° to the probe axis. For this measurement, the pressure difference between the central hole (measuring total stagnation pressure) and a series of additional holes arranged on the carbon fiber tube (measuring static pressure) were used to determine the approximate dynamic pressure at the probe tip. The pressure measured by this hole combination differs from the true dynamic pressure, Q , depending on the alignment of the wind vector with the probe axis. The two horizontally-opposed circumferential holes are arranged to produce a pressure difference which changes with the sideslip angle, β , of the air flow relative to the probe axis. Similarly, the two vertically-opposed circumferential holes were arranged to produce a pressure difference which changes with the angle of attack, α , of the air flow relative to the probe axis. Thus, Q , α and β can be determined by measuring the pressure differences across the different holes arranged on the probe.

Prior to installation on the HiDRON H2, the probe was calibrated in a wind tunnel to determine its directional response using an apparatus designed to pitch and yaw the probe at α and β angles up to 25° relative to the mean wind vector. Based off of established procedures, e.g. as outlined by Bohn and Simon (1975); Treaster and Yocum (1975); van der Kroonenberg et al. (2008) and Wildmann et al. (2014), and utilizing an implementation approach very similar to that used by Witte et al. (2017), the pressure differences at each α and β angle combination experienced during directional response calibration were used to build pressure coefficients

$$C_\beta(\alpha, \beta) = \frac{\Delta P_{32}}{\Delta P_1 + 0.5(\Delta P_{32} + \Delta P_5)} \quad (8a)$$

$$C_\alpha(\alpha, \beta) = \frac{\Delta P_{54}}{\Delta P_1 + 0.5(\Delta P_{32} + \Delta P_{54})} \quad (8b)$$

$$C_q(\alpha, \beta) = \frac{\Delta P_1 - Q}{\Delta P_1 + 0.5(\Delta P_{32} + \Delta P_{54})} \quad (8c)$$

195 where ΔP_1 is the pressure difference between the central hole and the static pressure, ΔP_{32} is the pressure difference across the horizontal probe holes, ΔP_{54} is the pressure difference across the vertical probe holes and Q is the dynamic pressure. The probe design resulted in unique combinations of C_β , C_α and C_q for each α and β angle of the probe to the relative air velocity vector. These relationships are stored in tables following the wind tunnel calibration.

To calculate the relative wind velocity vector measured during flight, C_α and C_β were calculated for every sample point from the measured ΔP_1 , ΔP_{32} and ΔP_{54} . Using the calibration tables, the values of α and β which produces that combination of C_α and C_β could be identified. A similar process was used to identify the corresponding value of C_q measured at that C_α and C_β combination, which allowed Q to be determined. The result is knowledge of the magnitude and direction of the dynamic pressure vector relative to the probe axis for every sampled combination of ΔP_1 , ΔP_{32} and ΔP_{54} . The dynamic pressure was then converted to velocity using the density determined from iMet-XF measurements of the ambient pressure, temperature and humidity.

The probe used on these flights was also heated to prevent ice formation within the probe during flight. This was accomplished by wrapping the probe body in nickel-chromium resistance wire. A feedback circuit, using a thermistor attached to the probe tip, passed current through the wire at a rate sufficient to maintain the probe tip temperature at 50°C. By repeating the wind tunnel directional response calibrations with and without heating active, it was determined that there was no influence of probe heating on ΔP_1 , ΔP_{32} and ΔP_{54} , or their dependence on α and β . These calibration checks were also conducted both at 20 m s⁻¹, which replicated the expected flight dynamic pressure of $Q \approx 200$ Pa, and at 5 m s⁻¹ to check for any Reynolds-number dependence of C_β , C_α and C_q .

To measure ΔP_1 , ΔP_{32} and ΔP_{54} , the probe was connected to differential pressure transducers through 50 cm of 1.75 mm diameter flexible polymer tubing. To ensure that the low-density conditions at flight altitude did not result in pressure differences below the sensitivity of an individual transducer, the measured pressure difference was converted to analog voltage using two different sets of transducers by teeing the tubing to each transducer set, i.e. a low and high sensitivity transducer was used for each pressure difference ΔP_1 , ΔP_{32} and ΔP_{54} . The low-sensitivity transducer set was comprised of TE Connected Measurements 4515-DS5A002DP differential pressure transducers with a 500 Pa range. The second transducer set was comprised of Allsensors DS-0368 differential pressure transducers with a 65 Pa range. Both sets of analog output voltages were linearly scaled relative to the maximum transducer range with a nominal span of 4.5V and 4.0V respectively. During flight, the autopilot maintained flight speeds sufficient to produce pressure differences well within the range of the low-sensitivity transducers (i.e. the dynamic pressure was maintained between 100 Pa and 200 Pa) which exceeded the range of the high sensitivity transducer connected to ΔP_1 . Hence, only the readings from the low-sensitivity sensors were used for data analysis. However, the high sensitivity transducers provided a means to estimate the uncertainty of the pressure measurement, as will be described later.

225 To convert the air velocity vector components relative to the probe axis into a frame of reference relative to the ground, an additional coordinate transformation was conducted using the aircraft's pitch, yaw, and roll angles as measured by the autopilot. Details of this process are provided in Witte et al. (2017) and are based off of procedures described in Lenschow (1972) for measurements using similar probes mounted on crewed aircraft. This process assumes that the coordinate system of the probe during wind tunnel calibration is perfectly aligned with the body-frame coordinate system of the autopilot, which is difficult to achieve in practice. Therefore, an additional procedure was used to correct for any misalignment of the probe axis and aircraft's body-frame axis. This approach, described in Al-Ghussain and Bailey (2021), also corrects for airframe influence on the measured Q , and time misalignment between the probe's pressure sensors and the aircraft's kinematic sensors.

230 As the autopilot and payload data acquisition systems were acquired asynchronously, alignment of autopilot kinematic data and five-hole-probe pressure data in time was conducted during post-processing by cross-correlating the dynamic pressure measured by the aircraft's intrinsic pitot probe (recorded by the autopilot along with the aircraft position and orientation information) and ΔP_1 of the five-hole probe recorded by the payload data acquisition system. The time lag between the two systems was then removed before performing the transformation of the velocity vector in the aircraft body frame to the Earth-fixed frame of reference. To do so, the aircraft position and orientation information was up-sampled from the autopilot's 10 Hz sample rate to the 1 kHz sample rate used by the on-board data acquisition system, with the up-sampling conducted using simple linear interpolation.

235 The result of these procedures is a time-dependent wind velocity vector described using components $u(t)$, $v(t)$, and $w(t)$ which are aligned to the East, to the North, and up, respectively. The time-dependent horizontal wind velocity magnitude and direction could then found from

$$U(t) = (u(t)^2 + v(t)^2)^{-0.5} \quad (9)$$

245 and

$$\gamma(t) = \text{atan2}(-u(t), -v(t)) \quad (10)$$

where atan2 indicates a numerical implementation of the \tan^{-1} function used to disambiguate the polar direction using the quadrant formed by the sign of the velocity components.

Note also that, although data was acquired at a 1 kHz sample rate to ensure that the infrasonic microphone response was fully resolved, the actual probe frequency response was much lower due to viscous attenuation of the pressure fluctuations within the tubing, coupled with inaccuracies introduced by high-frequency resonance within the transducer cavity (Grimshaw and Taylor, 2016). At ambient conditions, the frequency response was estimated to be on the order of 20 Hz using the same measurement approach utilized in Grimshaw and Taylor (2016) and Witte et al. (2017), which measures the response of the system following a step change in pressure. Similar response tests conducted in an environment chamber at -70°C and 8000 Pa indicated that, consistent with the model presented in Grimshaw and Taylor (2016), both the resonance in the transducer cavity and viscous attenuation can be expected to increase with altitude, resulting in a slightly lower response frequency of 10 Hz.

Finally, it should be mentioned that the ΔP_{54} pressure line was inadvertently disconnected during Flights 2 and 3, which was not discovered until after Flight 3. Therefore, for these flights, conversion of five-hole probe voltages was conducted with α provided by the aircraft's autopilot and determined from the angle between the true airspeed determined from the aircraft's pitot probe, and the vertical velocity determined by the aircraft's variometer. The definition of C_α and C_β used for directional calibration and recovery of Q and β were also modified to not include ΔP_{54} . While not ideal, we were able to verify that this approach was justified by analyzing the Flight 1 data with and without inclusion of ΔP_{54} . The average difference between the resulting $u(t)$, $v(t)$ and $w(t)$ values was found to be less than 0.25 m s^{-1} with the average difference in the Reynolds normal stresses found to be less than $0.09 \text{ m}^2 \text{ s}^{-2}$. Importantly, the altitude dependence of these quantities was preserved. Figures comparing the differences resulting from the processing methods are presented in Appendix A.

2.2.2 Infrasonic Microphone:

Infrasonic measurements of acoustic frequencies were conducted using an infrasonic microphone. For these tests a microphone and acoustic measurement system developed at NASA Langley Research Center was used. The microphone, shown in Fig. 1b, when coupled with a PCB Piezotronics 485M49 amplifier, was capable of infrasound (acoustic frequencies lower than 20 Hz) detection with a sensitivity of 115 mV Pa^{-1} (amplified to $\pm 10 \text{ V}$) having a power consumption of 35 mW and weight of 186 g. The geometry of the 38.1 mm diameter microphone diaphragm was designed with a high compliance (low diaphragm tension) such that membrane motion was substantially critically damped and optimally dimensioned for the 0.01 Hz to 20 Hz frequency range, with the full bandwidth of the sensor being 0.01 Hz to 1 kHz.

The microphone was mounted rigidly within the nose of the aircraft with the diaphragm plane normal to the forward flight direction. By being located within the fuselage, the microphone was protected by dynamic pressure fluctuations. As the wavelengths of infrasonic sound exceed 10 m, sound attenuation by the fuselage was not expected for frequencies lower than 20 Hz.

2.2.3 Data Acquisition:

A Measurement Computing Systems MCC USB-1608FS-Plus data acquisition system (DAQ) was used to digitize the voltage output from the pressure transducers and microphone signal conditioning unit. The DAQ also provided the 5 V signal used to power the pressure transducers. This particular DAQ was capable of recording eight single-ended analog inputs simultaneously at 16-bit resolution at rates of up to 400 kHz. During these experiments the DAQ sampled at 1 kHz the seven channels containing the analog voltage signals from all six pressure transducers and the infrasonic microphone. Digitized voltage values were then transferred through universal serial bus to the embedded computer for logging.

2.2.4 Embedded Computer:

The DAQ was connected via universal serial bus (USB) to a mini stick computer with an Intel Atom Z8350 processor, 128 GB eMMC non-volatile memory, and 4 GB RAM. To minimize radio frequency interference and shield the computer from high altitude radiation, the computer was encased in a copper shield (Fig. 3c). A custom script was used to control data acquisition

and storage. The computer stored all recorded data on its eMMC memory which was then downloaded post-flight via USB connection for archiving and further analysis. To allow payload operational verification during flight, an RS232 connection was established between the computer and the autopilot. Through this channel, sensor voltage variance and preliminary turbulence detection parameters were passed to the autopilot to be included in the telemetry stream. This information was also later available for preliminary temporal alignment of sensor and autopilot data.

To minimize the impact of electrical noise introduced into the pressure signals by the sensors and data acquisition system, during post-processing a background noise subtraction procedure was conducted on the digitized voltage signals prior to scaling them to Pascals. This process involved identifying a 5 minute long segment of the signal measured prior to balloon launch when a cover was present over the five-hole-probe (Fig. 1a) and the infrasonic signal was quiescent. This portion of the time series was assumed to be representative of the background electrical noise and therefore subtracted from the full time series in the Fourier domain in 5 minute long segments. This was done by conducting a Fourier transform on each segment and then subtracting the amplitude of the Fourier-transformed background-noise signal at each frequency, while preserving the phase information of the original segment. The filtered signal was then returned to the time domain by conducting an inverse Fourier transform.

2.3 Uncertainty Estimation of Wind Measurement

As described above, measurement of the wind vector was a multi-step process involving information from different sensors, calibrations and corrections. Therefore, to assess the uncertainty of the wind vector measurement, a Monte-Carlo method was used to estimate the error propagation from the sensors to the final wind estimate. To do so, the post-processing calculations were repeated for 100 iterations with each iteration having the sensor values perturbed from their measured value by an amount determined using normally-distributed random number generators. The standard deviation of the normal distributions were selected to correspond to each sensor's uncertainties.

Specifically, for a measured sensor value, here represented as $\Phi(t)$, a perturbed value $\Phi_i(t)$, was found for each iteration, i , following

$$\Phi_i(t) = \Phi(t) + \frac{E_B}{2}\mathcal{N} + \frac{E_P}{2}\mathcal{N}(t) \quad (11)$$

where \mathcal{N} represents a normally distributed random number, drawn from a standard normal distribution having mean of zero and standard deviation of unity. The quantities E_B or E_P represent the estimated bias (accuracy) and precision (resolution) errors for the sensor being perturbed, with the bias error perturbation, \mathcal{N} , added to $\Phi(t)$ only once per iteration, and the precision perturbation, $\mathcal{N}(t)$, added for every sample in time. Here E_B and E_P are taken to represent the 95% uncertainty range, twice the standard deviation of their distribution.

The analysis produced an ensemble of 100 time-dependent (and hence altitude-dependent) measurements of wind for each flight, randomly distributed via the propagation of the perturbed sensor readings, each perturbed following Equation 11. The uncertainty estimate was then found for the magnitude and direction from twice the ensemble standard deviation at each mea-

Table 1. Bias and precision errors for each sensor value used in wind estimate

Measured value	E_B	E_P
$\Delta P_1, \Delta P_{32}, \Delta P_{54}$	5 Pa	2 Pa
P	150 Pa	1 Pa
T	0.3 °C	0.01 °C
RH	5%	0.7%
yaw	0.2°	0.01°
pitch	0.2°	0.01°
roll	0.2°	0.01°
V_{G_x}, V_{G_y}	0.1 m s ⁻¹	0.02 m s ⁻¹

320 surement time, t , (corresponding to a 95% probability) of the 100 iterations. Note that this approach is similar to that employed by Van den Kroonenberg et al. (2008), but by employing the Monte-Carlo analysis this approach allows the uncertainty to vary in time (and hence altitude) as well as incorporating any additional uncertainty which may occur due to coupling of sensor errors.

The values for E_B and E_P used in the uncertainty propagation analysis are provided in Table 1 and required different 325 methods for their determination. For the pressure differences measured by the transducers connected to the five-hole-probe ($\Delta P_1, \Delta P_{32}, \Delta P_{54}$), E_B was estimated from the average difference between the low-sensitivity and high sensitivity ΔP_{32} and ΔP_{54} transducer values recorded during each flight, whereas E_P was estimated using twice the standard deviation of the difference. For P , T and RH , the manufacturer-provided accuracy and resolution values were used for E_B and E_P , respectively. Finally, the uncertainty of the attitude and heading reference system (AHRS) used by the autopilot was not 330 available, so the values for accuracy and resolution values from a different manufacturer's equivalent AHRS system were used as proxy values.

Note that this analysis does not take into account additional uncertainty introduced by errors in the directional calibration, misalignment in time between the sensors, and any altitude-dependent variability in the values provided in Table 1. To accommodate these undetected uncertainties in the analysis, the E_B and E_P values provided in Table 1 were doubled prior to 335 implementation in Equation 11.

The mean value of U across the 100 iterations at each time step is shown in Fig. 4a-c for Flights 1, 2 and 3, along with the corresponding 95% (two standard deviation) uncertainty bounds. The resulting uncertainty in the wind estimate was found to be altitude dependent, with the highest uncertainty of approximately 3.5 m s⁻¹ observed at the highest altitudes, decreasing to approximately 0.5 m s⁻¹ at the lowest altitudes measured. This altitude dependence directly arises from the influence of P , T and RH uncertainty on the air density estimate. Furthermore, although not directly apparent in Fig. 4, the uncertainty in wind 340 magnitude was found to be most dependent on the yaw angle, which is consistent with the observations of Van den Kroonenberg et al. (2008). The magnitude of the uncertainty present in Fig. 4 is consistent with the results of an intercomparison study

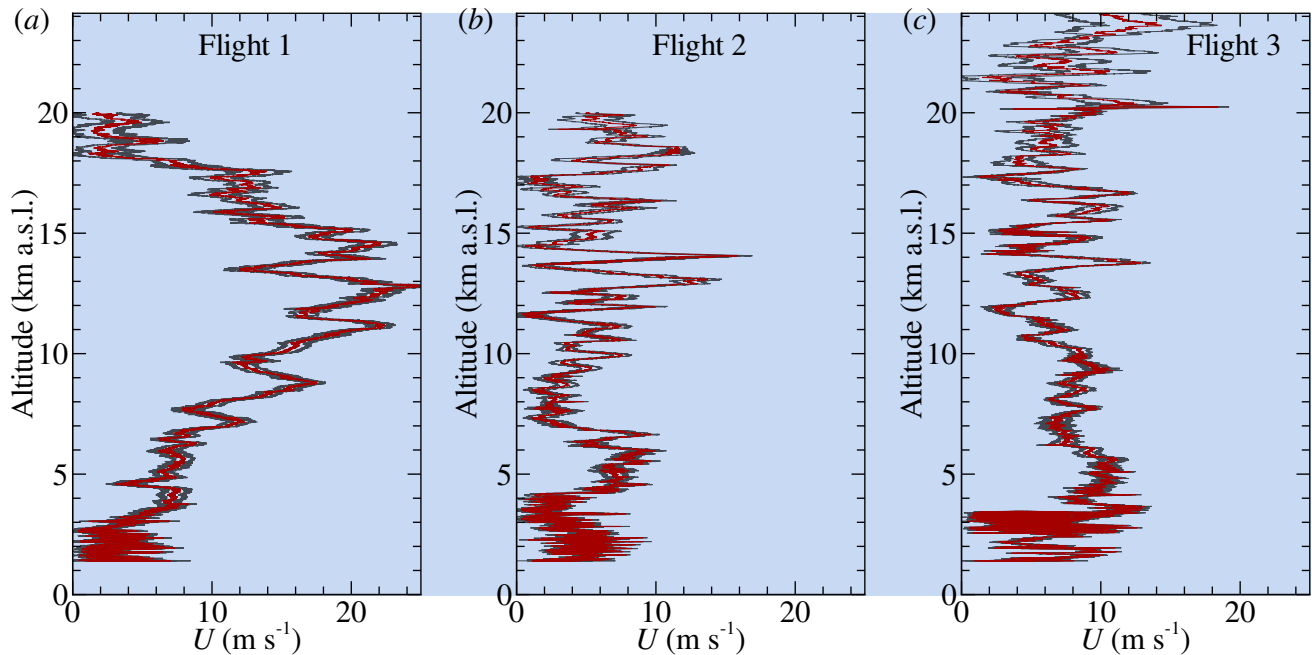


Figure 4. Result of uncertainty analysis for (a) Flight 1; (b) Flight 2; and (c) Flight 3. Red lines show velocity magnitude calculated from the mean of 100 ensembles, with corresponding 95% uncertainty bounds shown as black lines.

presented in Barbieri et al. (2019). In this study wind estimates from probes and procedures very similar to that used here were found to be within $\pm 1 \text{ m s}^{-1}$ of a ground-based reference velocity sensor.

345 2.4 Experiment Overview

350 The aircraft and payload combination was deployed in a measurement campaign conducted in the restricted airspace above Spaceport America, located near Truth or Consequences, New Mexico, U.S.A. between the Black Range and San Andres mountain ranges (Fig. 5), from June 1, 2021 through June 6, 2021. The height above sea level of launch and recovery of the aircraft was 1406 m above sea level (a.s.l.). Three flights were conducted by the HiDRON H2 on different dates, with Flight 1 being conducted on June 1; Flight 2 conducted on June 4; and Flight 3 being conducted on June 6. Each flight consisted of a weather-balloon carrying the glider aloft at an ascent rate of approximately 7 m s^{-1} to a release altitude of 25 km a.s.l. for Flights 1 and 2, and 30 km a.s.l. for Flight 3 (corresponding to $z = 23.6 \text{ km}$ and $z = 28.6 \text{ km}$ above ground level, a.g.l., respectively). After release from the balloon, the aircraft conducted an automated descent along a pre-determined flight path towards the Spaceport America runway. Autopilot-controlled approach, landing and recovery occurred on the Spaceport America main runway, at which point the aircraft, payload and all logged data were recovered.

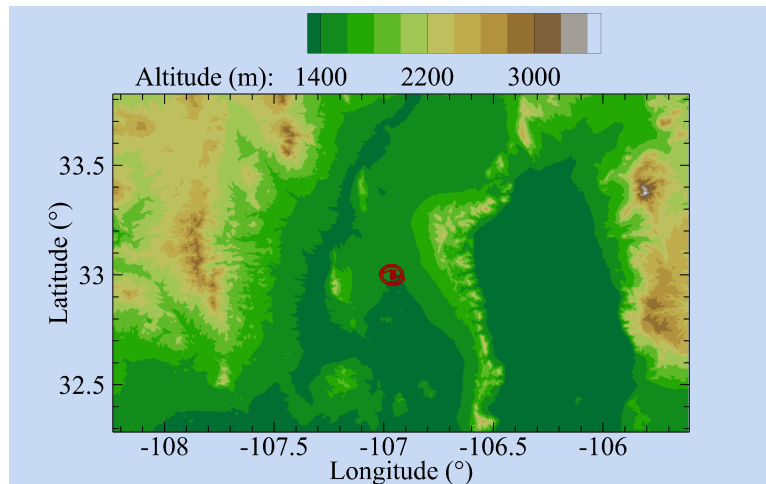


Figure 5. The topography of the flight area with Spaceport America with the trajectory of Flight 3 indicated by a red line to illustrate region of measurement.

2.5 Flight Profiles:

The flight trajectories for all three flights are presented in Fig. 6 showing balloon launch, ascent to 25 km or 30 km altitude a.s.l., release of the HiDRON H2 aircraft, controlled return to the airspace above the launch and control point, and helical descent to the landing point. The helical descent was conducted at an initial radius of approximately 5 km, selected as a compromise between optimizing aerodynamic efficiency of the aircraft in a turn (by minimizing the bank angle) and to stay in close proximity to the landing runway. As the aircraft descended, this radius was reduced to approximately 4 km and, eventually, 1 km to keep the aircraft within gliding distance of the designated landing point. During the descent phase of the flight, as shown in Fig. 2, the rate of descent decreased from 5 m s^{-1} to 1 m s^{-1} (producing a nominal descent rate of 2 m s^{-1}). Overall flight time was approximately 6 hours with 4 hours of that being the descent phase. Note that, during descent, several tests were conducted of the HiDRON H2's flight control system (including a test of autonomous soaring during Flight 3 which resulted in the aircraft gaining altitude for approximately 10 minutes). The result of these tests were occasional deviations of the flight path from the nominal helical trajectory.

All three flights started in the morning hours, with Flight 1 launched at 13:47 UTC (07:47 LT) on June 1 2021, released from the balloon at 14:35 UTC (08:35 LT), and landing at 18:42 UTC (12:42 LT). Flight 2 launched at 14:04 UTC (08:04 LT) on June 4 2021, released at 15:15 UTC (11:15 LT) and landed at 18:39 UTC (12:39 LT). Finally, Flight 3 launched at 14:07 UTC (08:07 LT) on June 6 2021, released at 15:17 UTC (09:17 LT), and landed at 19:43 UTC (12:43 LT). Local time, LT, at Spaceport America was Mountain Daylight Time (UTC -6:00).

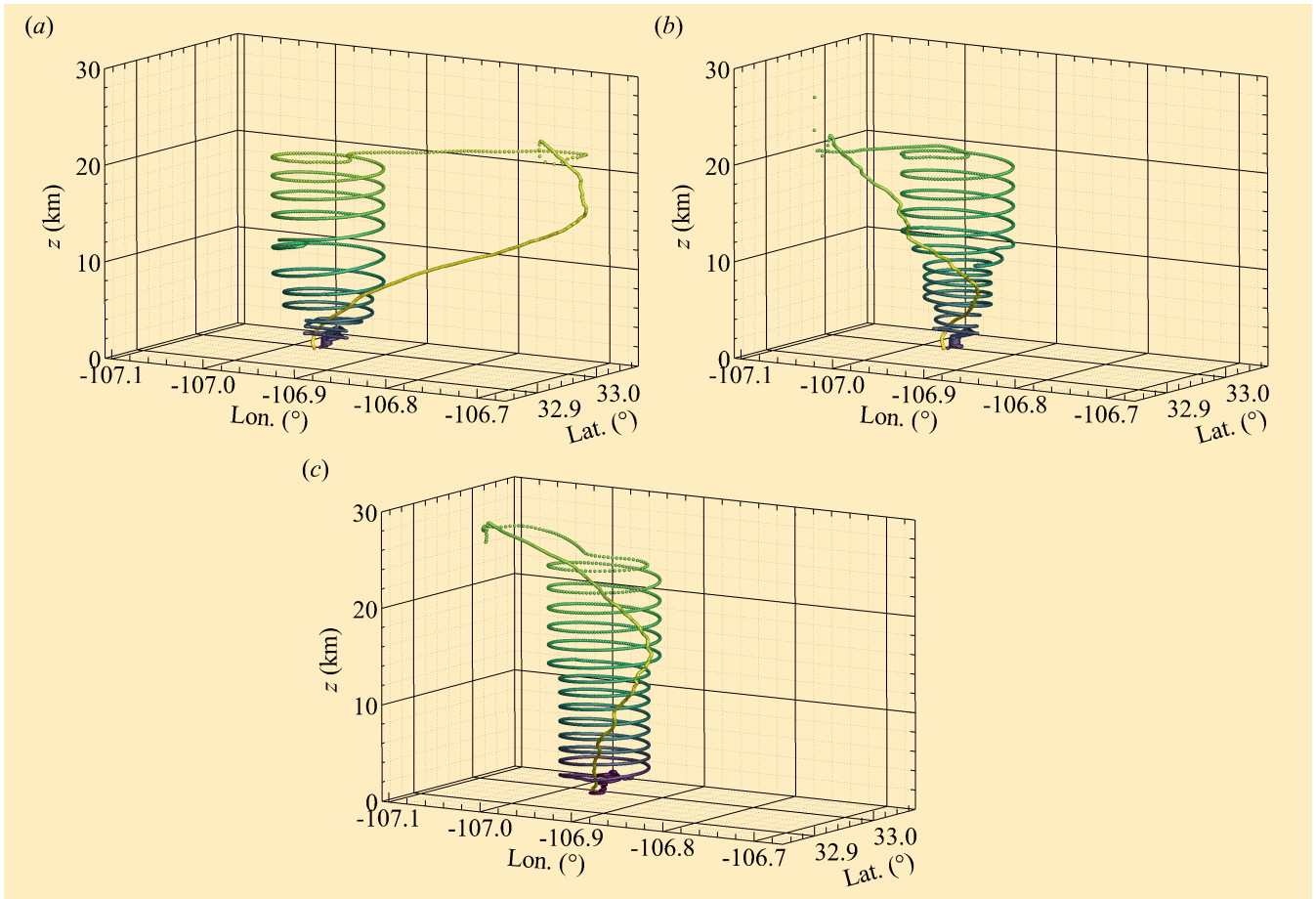


Figure 6. HiDRON H2 flight trajectory for (a) Flight 1, (b) Flight 2 and (c) Flight 3. Trajectory is colored by time, with lighter color indicating earliest phase of balloon ascent. z indicates height above ground level (a.g.l.).

3 Results

In this section, we present the measured values of temperature, relative humidity, wind vector, and infrasonic microphone
 375 signal amplitude, as well as presenting calculation approaches and results for selected statistics. Temperature and humidity
 sensors were mounted on the front side of the wing support pillar (as shown in Figure 1a) and during ascent they were in a
 stagnant region within the wing pillar wake and not sufficiently aspirated to prevent self-heating and delayed air exchange with
 the environment. Hence, only data from the controlled descent phase of the flight are presented for temperature and humidity
 in this section. Here, z is used to indicate the vertical distance referenced to ground level, i.e. above ground level (a.g.l.) with
 380 $z = 0$ corresponding to the launch and recovery altitude of 1406 m a.s.l.. In addition, when presenting results measured during
 descent we limit the data to $z < 20$ km for Flights 1 and 2 and $z < 25$ km for Flight 3, i.e. the portion of the flight when the
 aircraft was following a the helical trajectory (see Fig. 6) and within ± 5 km of a fixed geographic location. This latter constraint

is introduced since ΔP_1 exceeded the transducer's range shortly after the aircraft was released and started its flight towards the helical orbit location. By the time the aircraft reached the orbit location, ΔP_1 had returned to a measurable range.

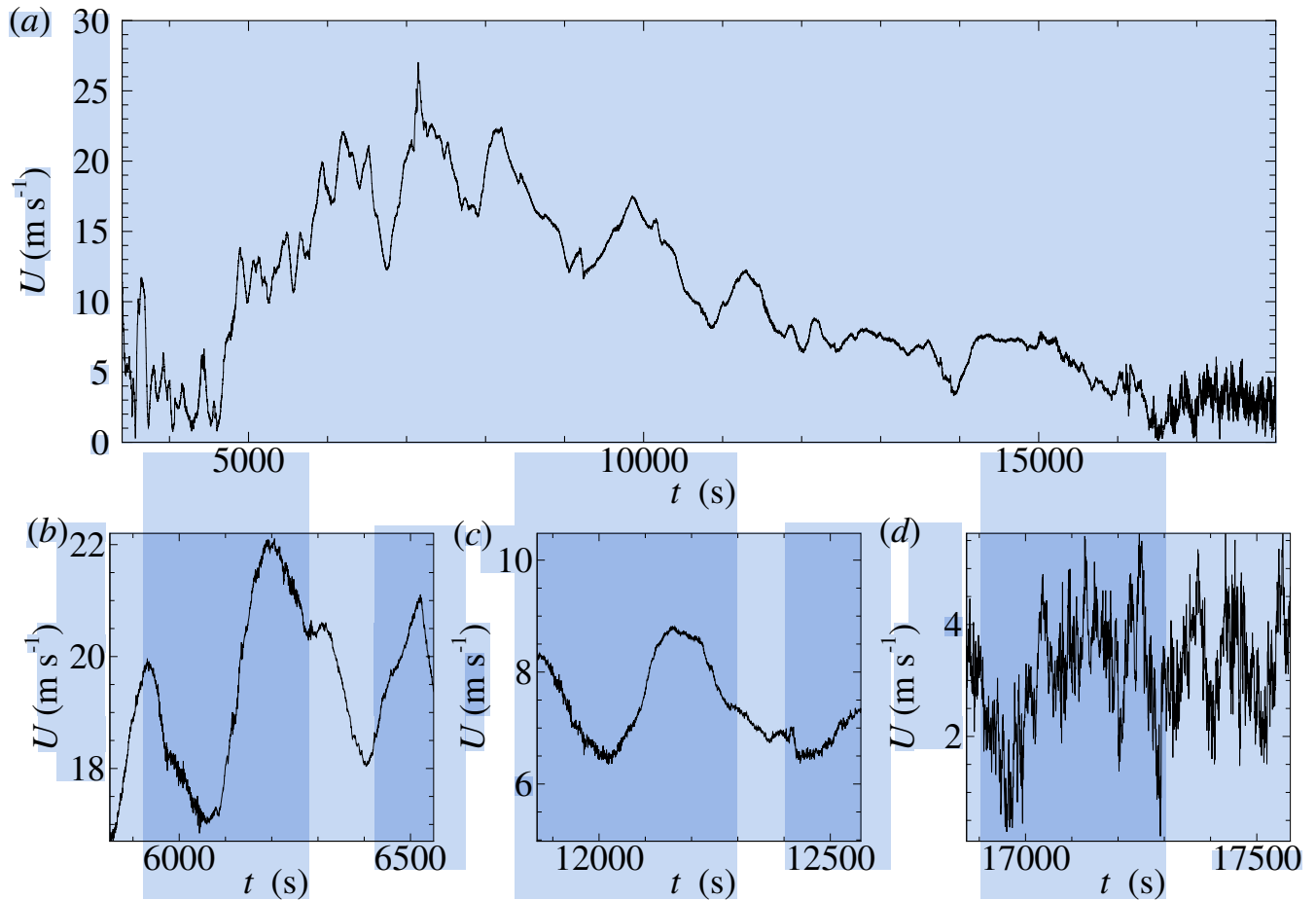


Figure 7. Time series of velocity magnitude low-pass-filtered at 1 Hz for (a) controlled descent portion of Flight 1 with $t = 0$ corresponding to startup of data acquisition system prior to balloon release. Subfigures (b), (c) and (d) show selected portions of time series in stratosphere, troposphere and boundary layer, respectively.

385 The time series of $U(t)$ measured during descent is presented in Fig. 7a. For this figure, the time series has been low-pass-filtered at 1 Hz to better visualize some of the features of the time series. By inspection, it was observed that while the aircraft was in the stratosphere ($t < 7000$ s), the velocity fluctuations were largely composed of low frequency motion having periods on the order of 400 s, as illustrated in the segment of the time series shown in Fig. 7b. For the nominal $|V_R|$ of approximately 60 m s^{-1} in this altitude range (see Fig. 2) this corresponds to wavelengths on the order of 24 km. Interspersed with these low frequency motions were irregular occurrences of high frequency fluctuations more characteristic of turbulence, such as shown in Fig. 7b around $t = 6000$ s. These latter events occurred in bursts lasting on the order of 100 s (or 6 km). As the aircraft descended through the troposphere, similar behavior was observed, although the duration of high-frequency

390

events were typically longer, on the order of 300 s (as illustrated in Fig. 7c around $t = 12000$ s and $t = 12500$ s). However, $|V_R| \approx 20$ m s⁻¹ at these altitudes so the corresponding lengths of these events remained near 6 km. Towards the end of the flight, the intensity and frequency of the high frequency occurrences increased (Fig. 7d), consistent with the UAS approaching and entering the boundary layer ($t > 16500$ s). Similar behavior was observed for Flights 2 and 3.

Following these observations, to capture the statistical properties of the high frequency portions of the time-series, the descent portion of the flight was divided into 3 km statistical segments, determined using $|V_R|\Delta t$, where Δt is the amount of time included in each segment. Due to the spiralling flight path (as illustrated in Fig. 6) each 3 km segment represents approximately 150 m of vertical descent. Quantities averaged over these segments use $\langle \rangle$ brackets, and we assume that the characteristics of the atmosphere within these segments are horizontally homogeneous (i.e. they are a function of z only). In order to decrease the vertical spacing between statistical values, each segment is overlapped with its neighbor by 50%, thereby decreasing the spacing of statistical quantities to 75 m vertically). Finally, to minimize the effects of low frequency bias on the statistics calculated for each segment, when statistics require the subtraction of a local mean value (e.g. as required to determine $u'(t)$, $v'(t)$ or $w'(t)$), rather than subtracting the segment's mean value, we instead subtract the linear trend within that segment (i.e. by detrending the segment).

3.1 Mean quantities

To establish the ambient conditions during each flight we averaged P , T , RH , U and γ over each statistical segment and compare vertical profiles of these quantities to publicly-available 12:00 UTC National Weather Service (NWS) radiosonde weather soundings launched from the El Paso (EPZ), Albuquerque (ABQ) and Tuscon (TUS) NWS forecast offices. These forecast offices and sounding times were selected due to their proximity to the launch site and flight times, with the launch site within the triangle formed by these three locations. To assist with comparison across sites in z , we have set $z = 0$ at 1406 m a.s.l. for all soundings. Furthermore, to assist with comparison, the National Oceanic and Atmospheric Administration (NOAA) upper air maps at 250 mbar and National Aeronautics and Space Administration (NASA) satellite imagery for the approximate time of Flights 1 through 3 are provided in Appendix B with the NWS sounding sites and Spaceport America (SPA) indicated on them. The NWS soundings employed Graw DFM-17 radiosondes with manufacturer-provided accuracies of $\pm 0.2^\circ\text{C}$ in temperature, $\pm 4\%$ in RH , ± 0.1 m s⁻¹ in wind speed and $\pm 1^\circ$ in wind direction.

Vertical profiles of $\langle T \rangle$ and $\langle RH \rangle$, measured by the HiDRON H2, are compared to the radiosonde profiles for all three flights in Fig. 8. The HiDRON H2 temperature is consistent with the trends produced by the radiosonde values, but shows a noticeable warm bias compared to the radiosondes for $z > 16$ km that appears most evident in the results from Flight 3. Note that no density or other correction was applied to this sensor measurement to account for the reduced convective heat transfer at these altitudes. The lapse-rate in the troposphere also appears to deviate from the radiosonde lapse rates for $z < 5$ km, although it is not clear if this is due to a sensor-related issue or due to spatial variability in the atmospheric conditions.

Figures 8d-f compare the corresponding $\langle RH \rangle$ measurements from the HiDRON H2 and NWS radiosondes. Significant differences are clearly evident among the profiles. However, noting that the radiosonde data were obtained from disparate locations up to 380 km away from the flight location, differences can be attributed to spatial heterogeneity in the atmospheric

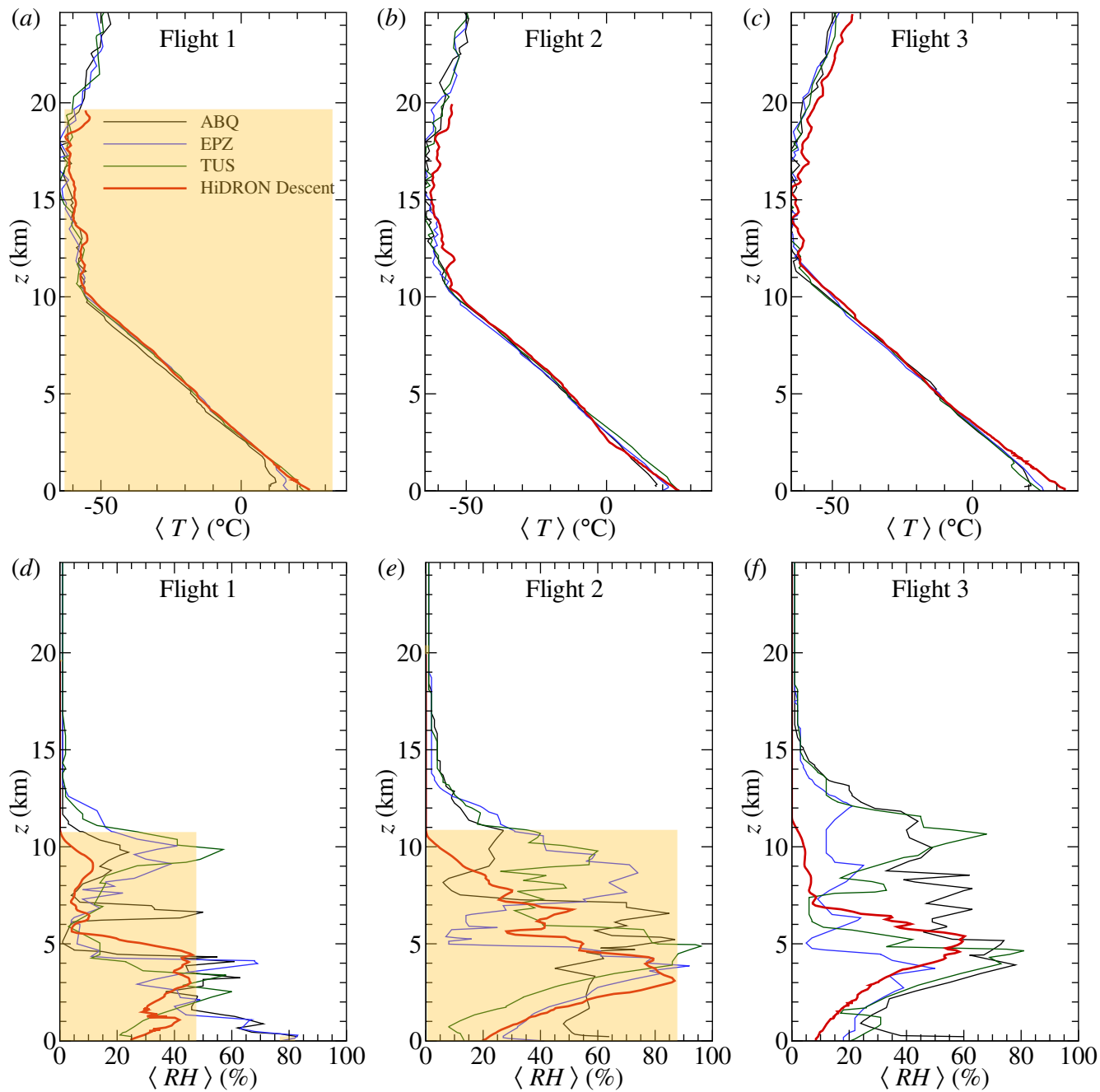


Figure 8. Temperature profiles measured during (a) Flight 1; (b) Flight 2; and (c) Flight 3 compared to NWS radiosonde soundings from the Albuquerque (ABQ), El Paso (EPZ), and Tuscon (TUS) forecast offices. Corresponding relative humidity profiles shown for (d) Flight 1; (e) Flight 2; and (f) Flight 3. ❌❌❌

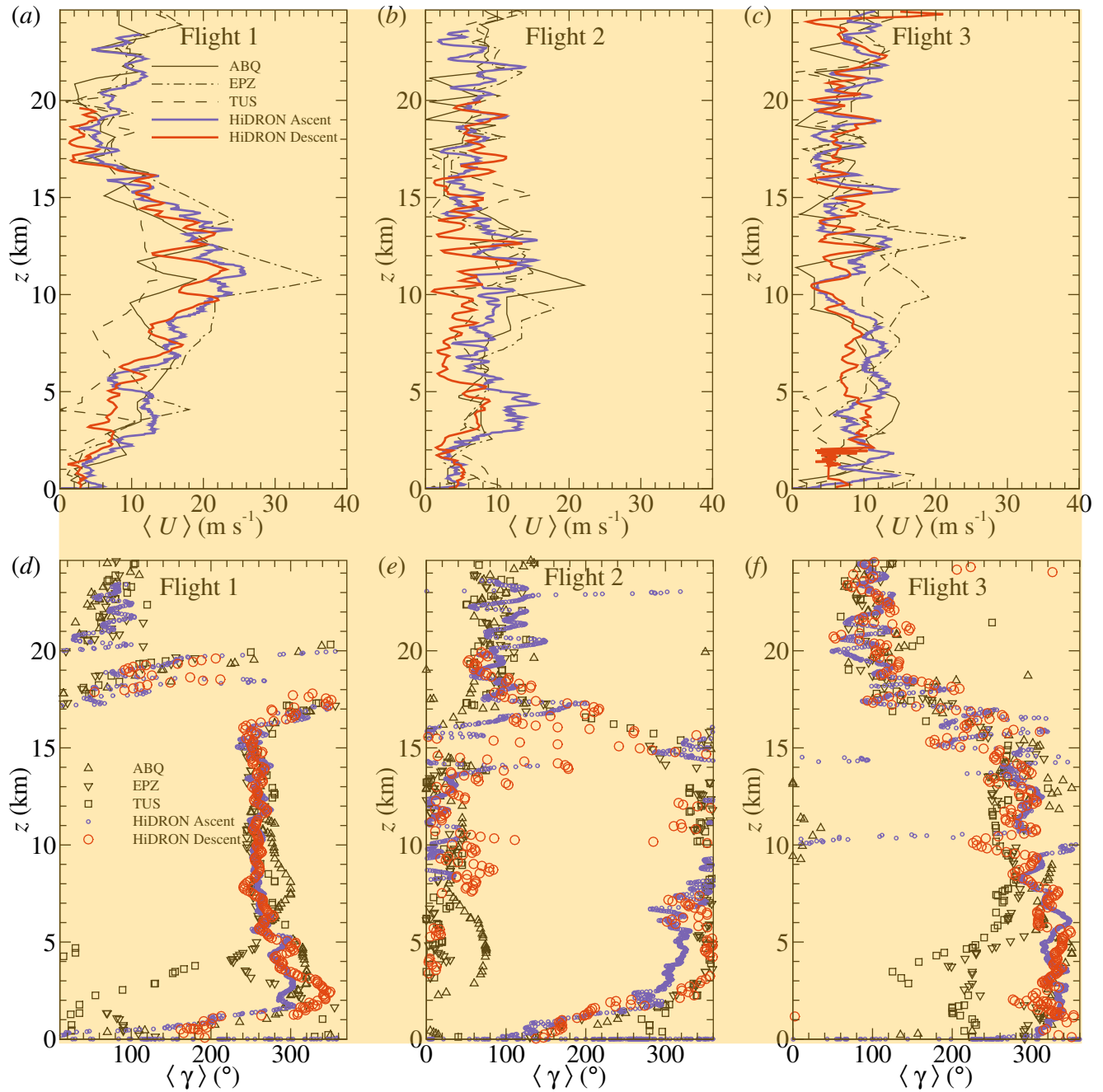


Figure 9. Horizontal wind magnitude a measured during (a) Flight 1; (b) Flight 2; and (c) Flight 3 compared to NWS radiosonde soundings from the Albuquerque (ABQ), El Paso (EPZ), and Tuscon (TUS) forecast offices. Corresponding wind direction shown for (d) Flight 1; (e) Flight 2; and (f) Flight 3.

moisture concentration. This is qualitatively illustrated by comparison of the cloud coverage in satellite observations (Appendix B). However, on all three days, the HiDRON H2 reported consistently lower RH values for $z > 7$ km, so a dry bias in the humidity sensor under cold conditions cannot be discounted.

430 The magnitude and direction of the horizontal winds for all three flights are shown in Fig. 9. In addition to comparison to the radiosonde soundings from ABQ, EPZ and TUS, we also compare the profiles measured during descent to those estimated from the ascent phase of each flight using (V_{G_x}, V_{G_y}) as measured by the autopilot's global positioning system (GPS). To mitigate any possible influence of pendulum motion of the aircraft on the balloon tether (estimated to have a natural period of approximately 5 s), the velocity values were filtered by applying a 25 s moving average. The resulting wind estimates
435 are treated as approximately equivalent to those produced by radiosondes, although the significantly increased weight of the aircraft relative to a radiosonde can be expected to produce a corresponding increase in the time constant compared to that of a radiosonde.

In general, the wind magnitude and direction measured by the HiDRON H2 are within the bounds provided by the radiosonde soundings, with the wind direction measured during descent producing good agreement with that reported by the radiosondes
440 and by the GPS on ascent. With respect to the wind magnitude, the HiDRON measurements do contain short wavelength fluctuations that were evident in both ascent (GPS ground velocity) and descent (five-hole-probe) velocity measurements made using the HiDRON. The significant difference between ascent and descent measurements are stronger long-wavelength fluctuations measured during descent than ascent for Flight 1 in the range $7.5 < z < 12.5$ km and for Flight 2 in the range $11 < z < 13$ km. These low frequency waves may be bias in the wind estimate introduced by the orbital path, but the magnitude
445 of the differences exceeds the anticipated uncertainty bounds presented in Fig. 4. Finally, differences in wind magnitude on the order of 5 m s^{-1} were observed between measurements made during ascent and descent in the troposphere during Flights 2 and 3. It is not clear what the source of this difference is, although there was a time difference of 2 to 4 hours between when the aircraft ascended through this region on its balloon and when it descended through the same region in a glide.

As illustrated in Figs. 8-9, atmospheric conditions were similar for Flights 2 and 3, which differed from Flight 1. The
450 strongest winds occurred during Flight 1, which had an environmental lapse rate of $8.4 \text{ }^\circ\text{C km}^{-1}$ (Fig. 8a) and winds coming from 270° , increasing with altitude to a peak value over 20 m s^{-1} just above the tropopause ($z = 12.5$ km), after which the magnitude decreased with increasing z to the stratospheric inversion near $z = 17$ km. This pattern of constant wind direction and high wind magnitude is consistent with the presence of a jet stream, and the NOAA upper air wind meteorological maps (e.g. as provided in Appendix B) indicate that during Flight 1 a tropical jet stream was centered to the southeast of the flight
455 location, over central Texas, such that the flight path was on the outer edge of the jet. The relative position of the jet stream for Flight 1 also explains the higher wind magnitudes measured at EPZ, which was closer to the center of the jet. Above the jet stream for Flight 1, the winds increase with altitude again, with significant directionality shift indicating horizontal shear was present above the temperature inversion.

The jet stream had moved to the east by the time of Flights 2 and 3 (as shown in Appendix B), which is reflected in the reduced
460 wind magnitude measured during these flights (Fig. 9b,e and Fig. 9c,f respectively), typically below $\langle U \rangle = 10 \text{ m s}^{-1}$. Wind direction was consistently from the north for $z < 15$ km for Flight 2, with directional shear observed between $z = 15$ km and

$z = 20$ km. An environmental lapse rate of $7.9 \text{ }^\circ\text{C km}^{-1}$ was measured for Flight 2 with a corresponding value of $8.2 \text{ }^\circ\text{C km}^{-1}$ measured for Flight 3. Wind observations during Flight 3 can be summarized as being nearly constant values of $\langle U \rangle \approx 10 \text{ m s}^{-1}$ up to $z = 30$ km, with winds coming from 300° in the troposphere backing with altitude to be from 100° at $z = 30$ km.

Turbulent Quantities

The HiDRON H2 measurements can be used to quantify the intensity of turbulence at different altitudes. For example through the turbulent kinetic energy, $\langle k \rangle$ which was calculated for each statistical segment using

$$\langle k \rangle = \frac{1}{2} (\langle u'^2 \rangle + \langle v'^2 \rangle + \langle w'^2 \rangle). \quad (12)$$

Note that since $u(t)$, $v(t)$ and $w(t)$ were oversampled, an additional filtering step was taken to minimize the influence of high-frequency noise on $\langle u'^2 \rangle$, $\langle v'^2 \rangle$, and $\langle w'^2 \rangle$. To do this, these quantities were calculated by integrating the corresponding velocity spectrum, $F_{uu}(f)$, $F_{vv}(f)$, and $F_{ww}(f)$ (equivalent to the one-sided autospectral density function of the detrended velocity component, following the terminology of Bendat and Piersol, 2000) over a specified frequency, f , range. The velocity spectra were found for each statistical segment using Welch's periodogram method implemented with a variance-preserving Hanning window, three subintervals, and a 50% overlap, implemented using the Matlab function 'pwelch'. The final low-pass filtered estimates of $\langle u'^2 \rangle$, $\langle v'^2 \rangle$ and $\langle w'^2 \rangle$ were then determined by integrating $F_{uu}(f)$, $F_{vv}(f)$ and $F_{ww}(f)$ over the frequency range where they were above the noise floor. This range was determined by inspection of the compensated spectra, $fF_{uu}(f)$, $fF_{vv}(f)$, and $fF_{ww}(f)$, which will reach a minimum at the frequency where the noise has a greater contribution to the integration than the signal. The filter frequency was consistent with the probe's frequency response in the boundary layer and varied between 1 Hz and 20 Hz above the boundary layer. Note that the Reynolds stresses filtered this way were found to be an average of 85% of the variance of the corresponding unfiltered signal, reflecting the influence of high frequency noise on statistics.

An additional metric that can be used to quantify turbulence is the turbulent kinetic energy dissipation rate, ε . Within equilibrium homogeneous turbulence, ε can be expected to scale with the rate of production of k , and within the inertial subrange it should scale with k and the wavenumber range of the inertial subrange. The dissipation rate is particularly useful for turbulent quantification in atmospheric turbulence for which the scale of the energy containing eddies may be quite large or ill-defined since ε can be determined from small-scale fluctuations, without requiring resolution of the low wavenumber turbulence.

As determination of ε using Equation 2 requires measurement of spatial gradients of velocity over distances on the order of the Kolmogorov scale, it is challenging to directly measure ε in the atmosphere without additional assumptions. Thus, indirect estimates of ε are usually employed. Here, we assume the presence of sufficiently high Reynolds number for the formation of an inertial subrange in the energy spectrum. Under such conditions, the one-dimensional longitudinal wavenumber velocity

spectrum in the inertial subrange is expected to follow a scaling such that

$$E_{\ell\ell}(\kappa_\ell) = 0.49\varepsilon^{2/3}\kappa_\ell^{-5/3} \quad (13)$$

as suggested by Kolmogorov (1941) using the one-dimensional Kolmogorov constant of 0.49 empirically determined by Sadowghi and Veeravalli (1994). κ_ℓ is the longitudinal wavenumber and the wavenumber velocity spectrum calculated using the velocity component parallel to κ_ℓ .

To determine $\langle\varepsilon\rangle$ within each statistical segment, $E_{\ell\ell}(\kappa_\ell)$ was estimated using the component of the wind velocity aligned with $-\mathbf{V}_R$. This was calculated by first rotating the (u, v, w) coordinate system from the east-north-up alignment to instead align u with an axis parallel to the velocity of the aircraft with the air, i.e. we define $u_\ell(t)$ as the component of the wind velocity vector found by projection of the wind velocity vector, \mathbf{U} , in the direction formed by $\langle-\mathbf{V}_R\rangle$. The velocity spectrum of $u_\ell(t)$ in the frequency domain, $F_{\ell\ell}(f)$, was then calculated on the rotated wind velocity vector following the same procedure used to calculate the Reynolds stresses. Noting that since Equation 13 is defined in the wavenumber domain, $F_{\ell\ell}(f)$ was then transformed to $E_{\ell\ell}(\kappa_\ell)$. To do this, the longitudinal wavenumber, κ_ℓ , was approximated using Taylor's frozen-flow hypothesis such that $\kappa_\ell \approx f2\pi|\langle\mathbf{V}_R\rangle|^{-1}$. We then found the longitudinal velocity spectrum in the wavenumber domain as $E_{\ell\ell} = F_{\ell\ell}|\langle\mathbf{V}_R\rangle|(2\pi)^{-1}$, where this last operation was conducted to ensure that

$$\int_0^\infty E_{\ell\ell}(\kappa_\ell)d\kappa_\ell = \langle u_\ell^2 \rangle. \quad (14)$$

Finally, Equation 13 was used to estimate $\langle\varepsilon\rangle$ by least-squares fit to $E_{\ell\ell}$. This fit was conducted over the κ_ℓ range corresponding to the frequency range used in the calculation of $\langle k \rangle$. The result is an estimate of ε for each statistical segment, i.e. $\langle\varepsilon\rangle$. Note that the approach used here provides only an approximation of $\langle\varepsilon\rangle$ as $E_{\ell\ell}(\kappa_\ell)$ will only follow Equation 13 in the presence of inertial turbulence, whereas the fit will always provide a non-zero value of $\langle\varepsilon\rangle$ even if no turbulence is present. Therefore, some caution is required when interpreting these values.

The values of $\langle k \rangle$ are compared to the corresponding values of $\langle\varepsilon\rangle$ in Fig. 10. Although there is significant scatter, the general trend follows the $\langle k \rangle \propto \langle\varepsilon\rangle^{2/3}$ expected for this calculation approach, demonstrating some intrinsic consistency in the different calculations. Note that, in addition to the implicit assumptions made when calculating $\langle\varepsilon\rangle$, due to the statistical segment length used for averaging, the value of $\langle k \rangle$ will be biased to wavelengths smaller than the statistical segment length and therefore may not completely describe the actual energy content of the turbulence.

The corresponding statistic of eddy dissipation rate, $EDR = \varepsilon^{1/3}$, is often used in the aviation industry to quantify turbulence. Following Huang et al. (2019), this metric allows the turbulence to be characterized as: steady for $EDR < 0.1$; weak for EDR between 0.1 and 0.3; moderate for EDR between 0.3 and 0.5; strong for EDR between 0.5 and 0.8; and very strong for $EDR > 0.8$. The measured profiles of $\langle k \rangle$ and $\langle EDR \rangle$ are compared to each other for all three flights in Figs. 11a, c, and e. For all flights, the $\langle EDR \rangle$ values indicate only weak turbulence was present. The most noticeable region of turbulence is just

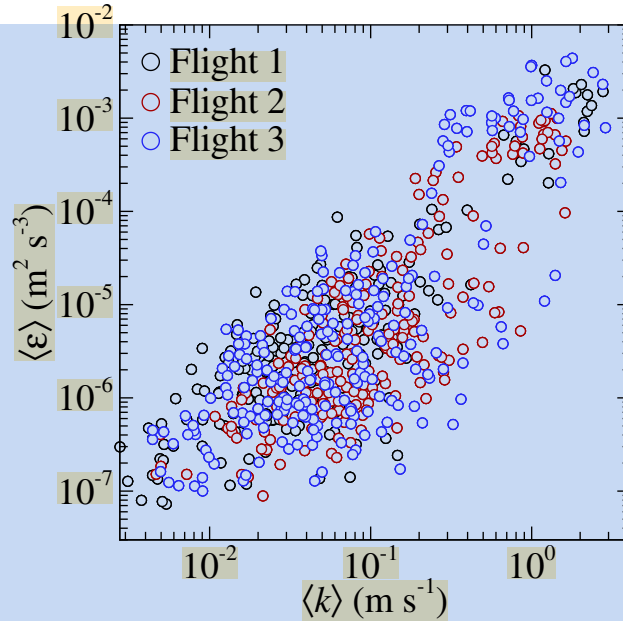


Figure 10. Comparison of turbulent kinetic energy and turbulent kinetic energy dissipation rate calculated within each statistical segment.

above and within the boundary layer, evident in Fig. 11a as an increase in $\langle k \rangle$ and $\langle EDR \rangle$ for $z < 2$ km, with slightly thicker regions of elevated $\langle k \rangle$ evident in Fig. 11b and c over the range $z < 4$ km and $z < 3$ km for Flights 2 and 3, respectively.

Above the boundary layer turbulence $\langle k \rangle$ and $\langle EDR \rangle$ are largely in agreement, although for stratospheric altitudes there are numerous localized regions where elevated $\langle k \rangle$ values were measured during Flights 2 and 3. To investigate these regions further we employ the continuous wavelet transform. This approach was used due to the co-existence of low-frequency and high-frequency motions (as observed in Fig. 7, for example) and therefore to avoid any bias introduced by the segment length, we utilize the wavelet transform's ability to discern the time/altitude dependence of these behaviors.

The continuous wavelet transform is

$$W(a, b) = \int_{-\infty}^{\infty} u_{\ell}(t) \frac{1}{a} \Psi^* \left(\frac{t-b}{a} \right) dt \quad (15)$$

where Ψ^* is the complex conjugate of the selected wavelet function, a is the scale parameter, and b the position parameter. The result of the transform is the wavelet coefficient, W , as a function of a and b which can be related to f and t , respectively. Here, the transform was implemented in Matlab using the analytical Morlet wavelet (Tavoularis, 2005) with the frequency range limited to 0.0001 Hz to 5 Hz (corresponding to the approximate frequency at which orbits were completed and the Nyquist frequency of the minimum probe response, respectively).

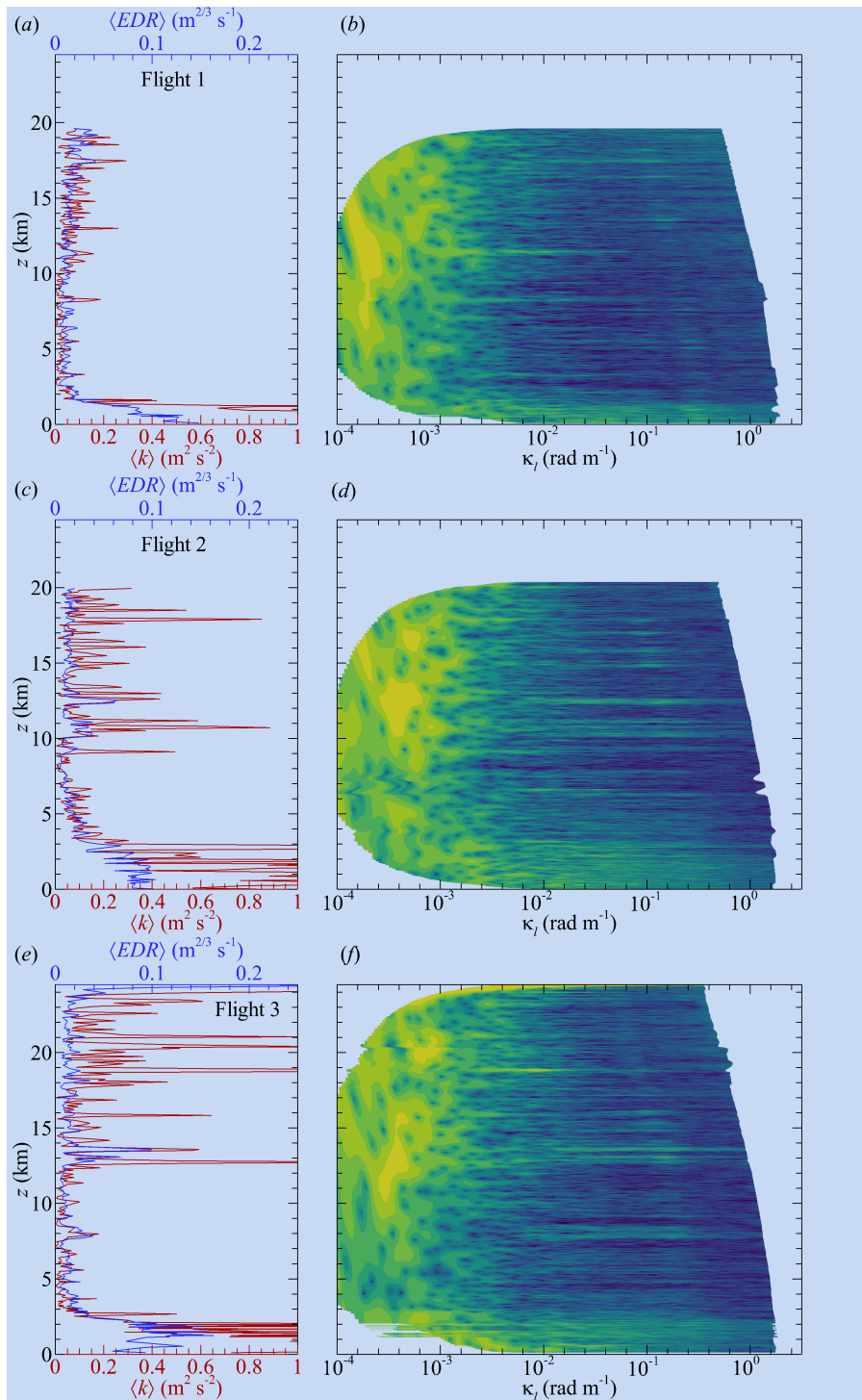


Figure 11. Profiles of $\langle k \rangle$ and $\langle EDR \rangle$ for (a) Flight 1, (c) Flight 2, and (e) Flight 3. Contours of the base 10 logarithm of the magnitude of wavelet coefficient are also shown for (b) Flight 1, (d) Flight 2, and (f) Flight 3 as functions of longitudinal wavenumber and z . Contour levels are the same in (b), (d) and (f).

Figures 11b, d, and f present the wavelet transform of $u_\ell(t)$ for Flights 1, 2 and 3 respectively. The results are presented as logarithmically-scaled isocontours of the complex modulus of the wavelet coefficient, $|W|$, as a function of $z(t)$ and $\kappa_\ell \approx f2\pi|\langle \mathbf{V}_R \rangle|^{-1}$. Noticeable in Figs. 11b, d, and f is the significant long wavelength content for $\kappa_\ell < 0.003$ (wavelengths larger than 2 km) when $z > 10$ km. This long wavelength content is the signature of the long period fluctuations in Fig. 7 and

540 fluctuations with altitude measured in Fig. 9.

High frequency content is also evident, not only in the proximity of the boundary layer but also in thin regions corresponding to altitudes where elevated $\langle k \rangle$ and $\langle EDR \rangle$ are observed in Figs. 11a, c, and e. For example, for Flight 1, distinct regions of elevated $|W|$ appear for $\kappa_\ell < 0.1$ at $z \approx 8$ km and $z \approx 12$ km and with higher wavenumber content around $z \approx 17$ km. The larger spikes in $\langle k \rangle$ measured during Flights 2 and 3 above $z = 10$ km appear to have contributions at both high wavenumbers

545 for $10 < z < 11$ km and $z \approx 12.5$ km and at low wavenumbers for $z > 15$ km. Similar behavior is also evident in the Flight 3 wavelet transform with the higher wavenumber content appearing around $z \approx 13$ km. Hence, the elevated $\langle k \rangle$ for $z > 15$ km in Figs. 11c and e appears to be due to low wavenumber contributions to $\langle k \rangle$.

3.3 Infrasonic Detection of Turbulence

To examine the effectiveness of infrasonic sensing for detecting atmospheric turbulence, we use the amplitude of the acoustic

550 signal measured by the microphone quantified using its variance, σ^2 . We note that σ^2 will include pressure waves generated by the long wavelength fluctuations shown in Fig. 11b, d, and f (which appear to contain significant energy content) as well as any inertial turbulence present and that this long wavelength motion will produce low frequency acoustic waves. Hence, we expand our segment length to 240 s (corresponding to the nominal time it took the HiDRON H2 to complete half an orbit) in order to ensure that the low frequency content is included in the variance calculation. Statistical averages calculated over this

555 longer segment size are indicated by $[\]$ brackets. Profiles of $[\sigma^2]$ measured during all three flights are presented in Fig. 12a-c.

Noticeably, there was a decrease in signal amplitude with increase in altitude measured in all cases. It was found that this decrease closely corresponds to the reduction in local atmospheric pressure, and therefore is attributed to increased atmospheric absorption due to the increase in molecular mean free path with altitude (Bass et al., 2007). Despite this altitude dependence, localized increases in $[\sigma^2]$ were observed, particularly near the boundary layer. When just the infrasonic portion of the acoustic

560 amplitude is isolated by integrating the microphone signal power spectrum over the range $f < 20$ Hz to obtain $[\sigma^2]_{LF}$, similar attenuation is evident as shown in Fig. 12a-c.

The altitude attenuation will be dependent on the local temperature as well as pressure hence the ratio $[\sigma^2]_{LF}/[\sigma^2]$, which represents the fraction of the microphone signal in the infrasonic range, can be used to compensate for the signal absorption with altitude (assuming uniform frequency response of the microphone with altitude). This ratio is compared to $[k]$, a proxy

565 the source strength of the acoustic signal, for all three flights in Fig. 12d-f. When viewed in this way, the resulting infrasonic amplitude profile can be observed to strongly correlate with $[k]$, and seems to be sensitive to the long wavelengths which were measured in the stratosphere and, to a lesser extent, in the proximity of the boundary layer. This normalization becomes less effective in proximity to the boundary layer most likely due to the increase in broadband turbulence observed in this region

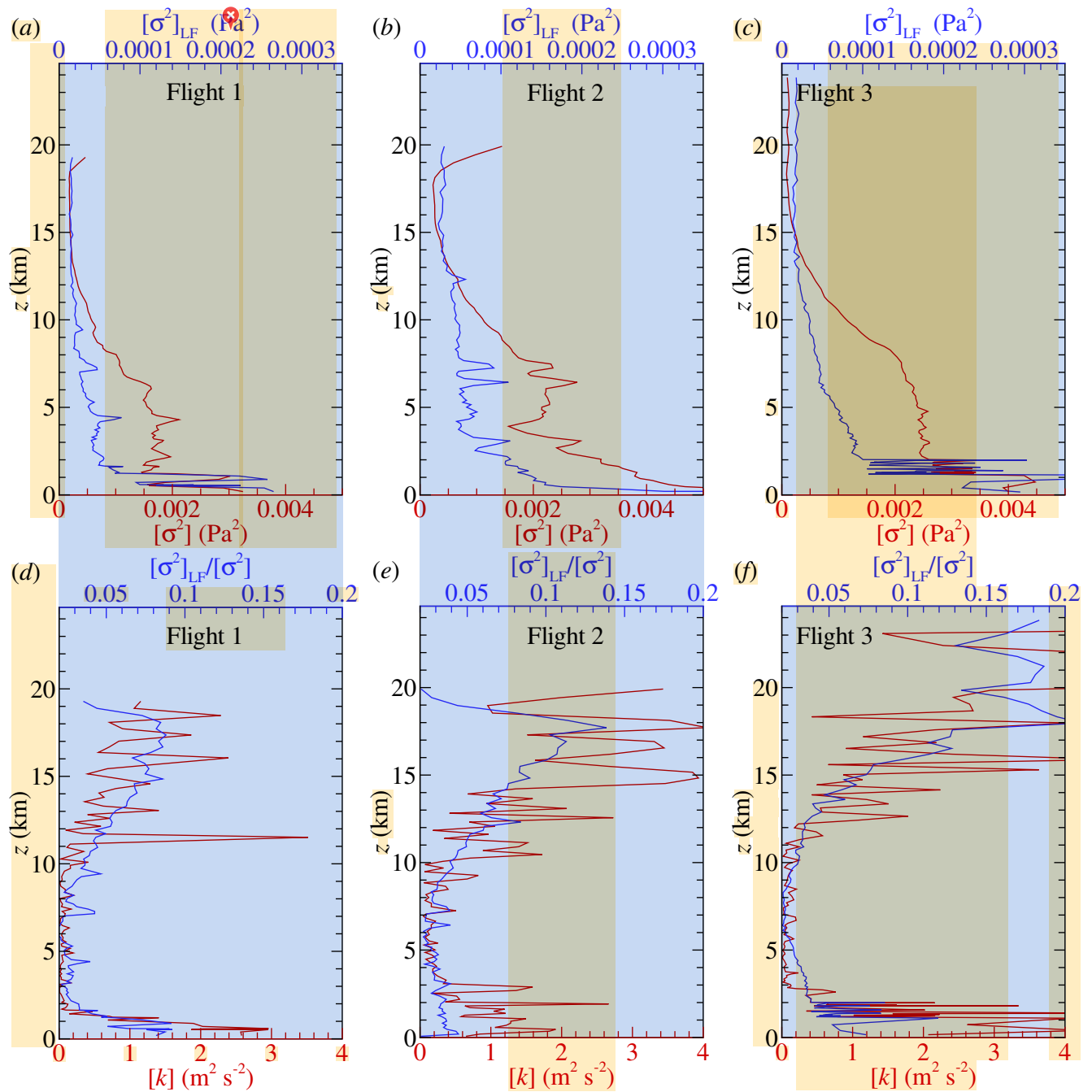


Figure 12. Infrasonic microphone signal as measured through its variance, $[\sigma^2]$, compared to variance of the signal low-pass-filtered at 20 Hz, $[\sigma^2]_{LF}$, for (a) Flight 1, (b) Flight 2, and (c) Flight 3. The ratio $[\sigma^2]_{LF}/[\sigma^2]$ compared to turbulent kinetic energy, $[k]$, for (d) Flight 1, (e) Flight 2, and (f) Flight 3.

resulting in increased high frequency content in the acoustic signal, thereby increasing $[\sigma]$ at the same rate as the $[\sigma_f]$ as can be observed in Fig. 12a-c.

3.4 Stability Conditions

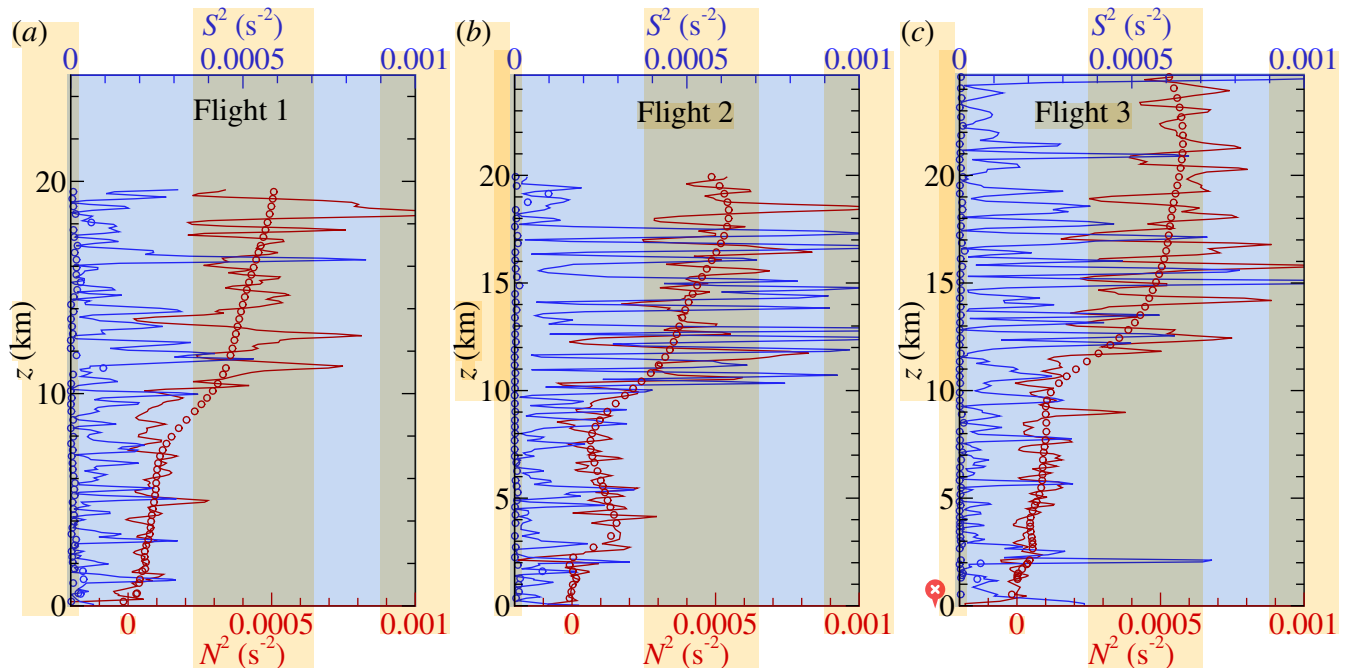


Figure 13. Square Brunt–Väisälä frequency, N^2 , and square shear frequency, S^2 , profiles for (a) Flight 1; (b) Flight 2; and (c) Flight 3. Solid lines show profiles calculated using vertical gradients calculated along flight trajectory, symbols show profiles calculated using vertical gradients calculated between neighboring orbits at same azimuthal position.

Profiles of the square Brunt–Väisälä frequency, N^2 , and square shear frequency, S^2 , provide some perspective about the altitude dependence of static stability and horizontal velocity shear, and hence potential for turbulence generation. However, approximating the mean vertical gradients of wind and virtual potential temperature required to calculate N^2 and S^2 using Equations 5 and 6 becomes somewhat ambiguous the HiDRON H2 measurements. This is due to the helical flight path, which introduces an increased sensitivity to horizontal gradients of U and θ_v compared to that of the vertical gradients.

Therefore, different approaches were attempted to calculate N^2 and S^2 . For the initial approach we present here, we assume horizontal homogeneity and attempt to replicate the expected response of a radiosonde to changes in the vertical wind structure, $\partial U/\partial z$. To do so, we assume a radiosonde time response for wind on the order of 40 s (Dirksen et al., 2014) which is introduced in commercial radiosondes by filtering of the pendulum effects and GPS noise, as well as the inertia of the balloon itself (Scoggins, 1965). This time response, when combined with a typical rise rate of 5 m s^{-1} , equates to a vertical resolution of approximately 200 m. Therefore, prior to calculating the vertical gradients, $u(t)$ and $v(t)$ were filtered using a moving average over a time span equivalent to a change in z of 200 m. The wind components $u(t)$, $v(t)$ and $\theta_v(t)$ were then averaged

over $\delta z = 100$ m bins (the approximate turbulent layer thickness estimated by Ko et al., 2019) prior to calculating the vertical
 585 gradients using these bin-averaged values. These values were then re-interpolated to each statistical segment.

The square Brunt–Väisälä frequency and square shear frequency calculated this way are presented as solid lines in Fig. 13
 for each flight. The results show large oscillations with altitude for all three flights, particularly in S^2 , which can be expected
 from Fig. 9. However, when $Ri = N^2/S^2$ is compared to both $\langle k \rangle$ and $\langle EDR \rangle$ as done in Fig. 14a and b respectively, the
 resulting trend is generally consistent with the expected behavior of increased turbulence intensity at low Ri . Specifically, the
 590 high turbulence intensity events (independent of whether quantified through $\langle k \rangle$ as done in Fig. 14a or $\langle EDR \rangle$ as done in
 Fig. 14b) largely occur when $Ri < 1$, although there are some instances of elevated turbulence when $Ri > 1$ and instances
 where no turbulence is evident when $Ri < 1$.

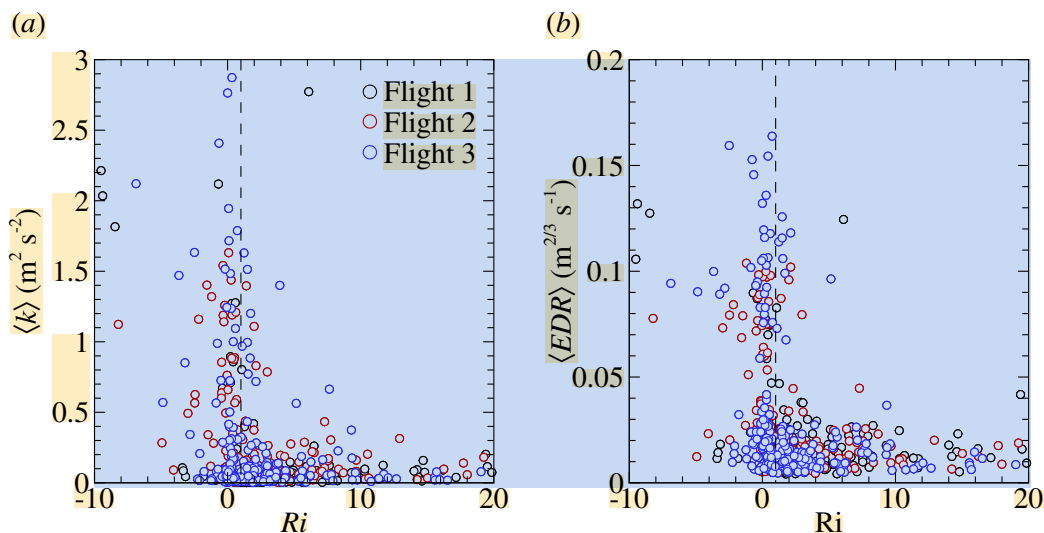


Figure 14. Comparison of (a) turbulent kinetic energy, $\langle k \rangle$, and (b) eddy dissipation rate, $\langle EDR \rangle$, to gradient Richardson number, Ri , calculated along flight trajectory. Dashed vertical line indicates $Ri = 1$.

As the helical descent of the aircraft results in approximately 1500 m of horizontal travel for every 100 m of decent, hor-
 izontal variability in the measured variables have an outsized impact on the calculation of Ri . In an attempt to eliminate the
 595 required assumption of horizontal homogeneity for the calculation of Ri , an alternative approach was attempted to calculate
 vertical gradients whereby the vertical profiles were expanded along the circumference of the aircraft's orbit. For each statisti-
 cal segment the two nearest segments in the z direction were used to calculate the vertical gradients using central differencing.
 In this way, the gradients were calculated vertically across individual orbits, rather than along the helical path. However this
 results in a gradient calculation with a vertical scale of the same order as the pitch of the helix, which was approximately
 600 2.5 km and therefore much larger than the thickness of the layers of turbulence observed in Fig. 11.

The values of S^2 and N^2 calculated this way are shown using symbols on Fig. 13a-c. This calculation approach effectively
 reproduces the N^2 profiles calculated along the flight path, but contains fewer fluctuations, particularly for $z > 10$ km. The

corresponding S^2 profiles, however, were an order of magnitude smaller when calculated across the orbits than when calculated along the flight path (reflected in the values near zero in Fig. 13a-c) and therefore resulted in Ri values on the order of 10^3 . The lower values of S^2 when calculated between the orbits likely reflects the larger vertical distances involved in the differencing across the orbits which will effectively filter out many of the vertical wind gradients shown in Fig. 9a-c. This approach is presented here as it may be more successful for flight trajectories with smaller orbit diameter, and smaller vertical pitch between orbits.

4 Summary and Conclusions

This report describes a balloon-launched glider UAS and instrumentation intended for measuring the statistical structure of atmospheric turbulence. To conduct these measurements, the aircraft was equipped with a five-hole-probe for measuring the three-component wind vector, and pressure, temperature and humidity sensors integrated into the aircraft.


These instruments allowed the measurement of vertical profiles of T , RH , U and γ up to $z = 25$ km above ground level. These profiles compared favorably with the nearest publicly-available National Weather Service radiosonde data for T and RH , although there were some noticeable differences in the RH values, which were lower than the radiosonde values for $z > 7$ km. There were also indications that additional corrections may be needed to T within the stratosphere. Wind profiles were in good agreement with the available National Weather Service radiosonde profiles, however comparison with the GPS-derived wind velocity measured during ascent provided the best comparison to the profiles measured during descent.

The descent trajectory allowed for the calculation of $\langle k \rangle$ and $\langle \varepsilon \rangle$ over a large horizontal wavelength range with high vertical resolution. The resulting vertical profiles suggest that isolated regions of weak turbulence were present in all three flights, and by examining the wavelet transform of the longitudinal velocity it was observed that these isolated regions could have different wavelength content depending on altitude. The wavelet transforms also indicated that long-wavelength fluctuations provided a significant contribution to the energy content for $z > 10$ km. These long-wavelength fluctuations were also picked up as low-frequency acoustic energy measured by an on-board infrasonic microphone. The microphone also detected an increase in broadband acoustic energy as the UAS approached the boundary layer, consistent with the more broadband frequency content of the turbulence within it. The results of this study therefore suggest that the infrasonic microphone can detect turbulent features, particularly near the stronger boundary layer turbulence.

An attempt was also made to calculate the gradient Richardson number from the temperature and wind profiles, however the helical flight trajectory of the UAS introduces ambiguity in the time and length scales used for determining the mean vertical gradients. A method was proposed which smoothed the wind velocity prior to calculating the gradients across 100 m vertical increments. This resulted in gradient Richardson numbers that corresponded to enhanced $\langle k \rangle$ and $\langle \varepsilon \rangle$ when $Ri < 1$, however there were outliers which suggested improvements could be made to the calculation approach. An alternative approach was presented which calculated the vertical gradients across the pitch of the helical flight path. This produced similar results for N^2 , however the S^2 results were an order of magnitude smaller due to the pitch being on the order of 2.5 km. The result was very high Ri values that predicted stable conditions even when turbulence was present.


Despite this ambiguity, these initial flights suggest the potential exists for this measurement approach to be used for high altitude turbulence research, for example enabling detailed analysis of length scales and anisotropy of the turbulence. However, additional flights will be beneficial for assessing the capabilities of this measurement technique. For example, for the three flights considered here, the turbulence above the boundary layer was relatively weak and limited in occurrence. Measurements
640 in more unstable conditions would lead to increased opportunities to conduct turbulent observations. Furthermore, flight patterns can be designed to allow examination of potential inhomogeneity of the statistics, for example by taking advantage of the helical trajectory taken by the glider during its descent to produce depictions of the horizontal heterogeneity of measured statistics. Additional flight patterns can also be designed with tighter helical descent can be designed to better calculate gradient Richardson number, with higher vertical resolution. Finally, improvements can be made to the data acquisition system
645 that would lessen the signal-to-noise ratio of the acquisition system, simplifying post-processing of the measurements and providing higher resolution of instances of any turbulence encountered.

Data availability. Data from these flights are available from the corresponding author on request.

 *Video supplement.* A video compilation of aircraft preparation, flight and recovery is publicly available at <https://vimeo.com/568101900>

Author contributions. S.B., G.P., N.C. planned the experiment which was realized by S.B., R.N., G.P. and A.S.. Data analysis was conducted
650 by A.H. and S.B. who also prepared the initial draft of the manuscript with input from the remaining authors.

Competing interests. The authors declare no competing interests are present.

 *Acknowledgements.* Financial support for this work was provided by NASA under the Flight Opportunities Program through award number 80NSSC20K0102 with Paul A. De León as the NASA Technical Officer. The authors would also like to dedicate this work to Dr. Qamar Shams who worked at NASA Langley Research Center and graciously assisted with the implementation and the loan of the infrasonic
655 microphone from NASA.

References

- Abarbanel, H. D. I., Holm, D. D., Marsden, J. E., and Ratiu, T.: Richardson Number Criterion for the Nonlinear Stability of Three-Dimensional Stratified Flow, *Phys. Rev. Lett.*, 52, 2352–2355, <https://doi.org/10.1103/PhysRevLett.52.2352>, 1984.
- 660 Al-Ghussain, L. and Bailey, S. C. C.: An approach to minimize aircraft motion bias in multi-hole probe wind measurements made by small unmanned aerial systems, *Atmospheric Measurement Techniques*, 14, 173–184, <https://doi.org/10.5194/amt-14-173-2021>, 2021.
- Al-Ghussain, L. and Bailey, S. C. C.: Uncrewed Aircraft System Measurements of Atmospheric Surface-Layer Structure During Morning Transition, *Boundary-Layer Meteorology*, 185, 229–258, <https://doi.org/10.1007/s10546-022-00729-2>, 2022.
- Alisse, J.-R., Haynes, P. H., Vanneste, J., and Sidi, C.: Quantification of stratospheric mixing from turbulence microstructure measurements, *Geophysical Research Letters*, 27, 2621–2624, <https://doi.org/https://doi.org/10.1029/2000GL011386>, 2000.
- 665 Bailey, S. C. C., Canter, C. A., Sama, M. P., Houston, A. L., and Smith, S. W.: Unmanned aerial vehicles reveal the impact of a total solar eclipse on the atmospheric surface layer, *Proceedings of the Royal Society A: Mathematical, Physical and Engineering Sciences*, 475, 20190212, <https://doi.org/10.1098/rspa.2019.0212>, 2019.
- 670 Bailey, S. C. C., Sama, M. P., Canter, C. A., Pampolini, L. F., Lippay, Z. S., Schuyler, T. J., Hamilton, J. D., MacPhee, S. B., Rowe, I. S., Sanders, C. D., Smith, V. G., Vezzi, C. N., Wight, H. M., Hoagg, J. B., Guzman, M. I., and Smith, S. W.: University of Kentucky measurements of wind, temperature, pressure and humidity in support of LAPSE-RATE using multisite fixed-wing and rotorcraft unmanned aerial systems, *Earth System Science Data*, 12, 1759–1773, <https://doi.org/10.5194/essd-12-1759-2020>, 2020.
- Balsley, B. B., Lawrence, D. A., Woodman, R. F., and Fritts, D. C.: Fine-scale characteristics of temperature, wind, and turbulence in the lower atmosphere (0–1,300 m) over the south Peruvian coast, *Boundary-Layer Meteorology*, 147, 165–178, 2013.
- 675 Balsley, B. B., Lawrence, D. A., Fritts, D. C., Wang, L., Wan, K., and Werne, J.: Fine Structure, Instabilities, and Turbulence in the Lower Atmosphere: High-Resolution In Situ Slant-Path Measurements with the DataHawk UAV and Comparisons with Numerical Modeling, *Journal of Atmospheric and Oceanic Technology*, 35, 619–642, <https://doi.org/10.1175/JTECH-D-16-0037.1>, 2018.
- Barat, J. and Bertin, F.: Simultaneous Measurements of Temperature and Velocity Fluctuations Within Clear Air Turbulence Layers. Analysis of the Estimate of Dissipation Rate by Remote Sensing Techniques, *Journal of the Atmospheric Sciences*, 41, 1613–1619, [https://doi.org/10.1175/1520-0469\(1984\)041<1613:SMOTAV>2.0.CO;2](https://doi.org/10.1175/1520-0469(1984)041<1613:SMOTAV>2.0.CO;2), 1984.
- 680 Barbieri, L., Kral, S. T., Bailey, S. C. C., Frazier, A. E., Jacob, J. D., Reuder, J., Brus, D., Chilson, P. B., Crick, C., Detweiler, C., Doddi, A., Elston, J., Foroutan, H., González-Rocha, J., Greene, B. R., Guzman, M. I., Houston, A. L., Islam, A., Kempainen, O., Lawrence, D., Pillar-Little, E. A., Ross, S. D., Sama, M. P., Schmale, D. G., Schuyler, T. J., Shankar, A., Smith, S. W., Waugh, S., Dixon, C., Borenstein, S., and de Boer, G.: Intercomparison of Small Unmanned Aircraft System (sUAS) Measurements for Atmospheric Science during the LAPSE-RATE Campaign, *Sensors*, 19, <https://doi.org/10.3390/s19092179>, 2019.
- 685 Bärffuss, K., Pätzold, F., Altstädter, B., Kathe, E., Nowak, S., Bretschneider, L., Bestmann, U., and Lampert, A.: New setup of the UAS ALADINA for measuring boundary layer properties, atmospheric particles and solar radiation, *Atmosphere*, 9, <https://doi.org/10.3390/atmos9010028>, 2018.
- Bass, H. E., Hetzer, C. H., and Raspert, R.: On the speed of sound in the atmosphere as a function of altitude and frequency, *Journal of Geophysical Research: Atmospheres*, 112, <https://doi.org/https://doi.org/10.1029/2006JD007806>, 2007.
- 690 Bendat, J. S. and Piersol, A. G.: *Random Data : Analysis and Measurement Procedures*, Wiley Interscience, New York, U.S.A., 3rd edn., 2000.

- Bertin, F., Barat, J., and Wilson, R.: Energy dissipation rates, eddy diffusivity, and the Prandtl number: An in situ experimental approach and its consequences on radar estimate of turbulent parameters, *Radio Science*, 32, 791–804, <https://doi.org/https://doi.org/10.1029/96RS03691>, 1997.
- 695 Bohn, D. and Simon, H.: Mehrparametrische Approximation der Eichräume und Eichflächen von Unterschall- bzw. Überschall-5-Loch-Sonden, *tm-Technisches Messen*, 468, 81–89, 1975.
-  Bowman, D. C. and Lees, J. M.: Infrasound in the middle stratosphere measured with a free-flying acoustic array, *Geophysical Research Letters*, 42, <https://doi.org/10.1002/2015GL066570>, 2015.
- 700 Calmer, R., Roberts, G. C., Preissler, J., Sanchez, K. J., Derrien, S., and O’Dowd, C.: Vertical wind velocity measurements using a five-hole probe with remotely piloted aircraft to study aerosol–cloud interactions, *Atmospheric Measurement Techniques*, 11, 2583–2599, <https://doi.org/10.5194/amt-11-2583-2018>, 2018.
-  Chunchuzov, I. P., Kulichkov, S. N., Popov, O. E., and Perepelkin, V. G.: Infrasound generation by meteorological fronts and its propagation in the atmosphere, <https://doi.org/10.1175/jas-d-20-0253.1>, 2021.
- 705 Clayson, C. A. and Kantha, L.: On Turbulence and Mixing in the Free Atmosphere Inferred from High-Resolution Soundings, *Journal of Atmospheric and Oceanic Technology*, 25, 833 – 852, <https://doi.org/10.1175/2007JTECHA992.1>, 2008.
- Cunningham, P. and Keyser, D.: SYNOPTIC METEOROLOGY | Jet Streaks, in: *Encyclopedia of Atmospheric Sciences (Second Edition)*, edited by North, G. R., Pyle, J., and Zhang, F., pp. 359–369, Academic Press, Oxford, second edition edn., <https://doi.org/https://doi.org/10.1016/B978-0-12-382225-3.00187-0>, 2015.
-  Cuxart, J., Tatrai, D., Weidinger, T., Kircsi, A., Józsa, J., and Kiss, M.: Infrasound as a Detector of Local and Remote Turbulence, *Boundary-Layer Meteorology*, 159, 185–192, <https://doi.org/10.1007/s10546-015-0100-2>, 2015.
- 710 Dirksen, R. J., Sommer, M., Immler, F. J., Hurst, D. F., Kivi, R., and Vömel, H.: Reference quality upper-air measurements: GRUAN data processing for the Vaisala RS92 radiosonde, *Atmospheric Measurement Techniques*, 7, 4463–4490, <https://doi.org/10.5194/amt-7-4463-2014>, 2014.
- D’Oliveira, F., Melo, F., and Devezas, T.: High-Altitude Platforms - Present Situation and Technology Trends, *Journal of Aerospace Technology and Management*, 8, 249–262, <https://doi.org/10.5028/jatm.v8i3.699>, 2016.
- 715 Egger, J., Bajrachaya, S., Heingrich, R., Kolb, P., Lammlein, S., Mech, M., Reuder, J., Schäper, W., Shakya, P., Shween, J., and H., W.: Diurnal Winds in the Himalayan Kali Gandaki Valley. Part III: Remotely Piloted Aircraft Soundings, *Mon. Wea. Rev.*, 130, 2042–2058, 2002.
- Ehrenberger, L. J.: Stratospheric Turbulence Measurements and Models for Aerospace Plane Design, Tech. Rep. TM-104262, NASA, 1992.
- 720 Enlich, R. and Mancuso, R.: The Turbulence Climatology of the United States between 20,000 and 45,000 Feet Estimated from Aircraft Reports and Meteorological Data, Tech. rep., Stanford Research Institute, <https://apps.dtic.mil/sti/pdfs/AD0672988.pdf>, 1968.
-  Fukao, S., Yamanaka, M. D., Ao, N., Hocking, W. K., Sato, T., Yamamoto, M., Nakamura, T., Tsuda, T., and Kato, S.: Seasonal variability of vertical eddy diffusivity in the middle atmosphere: 1. Three-year observations by the middle and upper atmosphere radar, *Journal of Geophysical Research: Atmospheres*, 99, 18 973–18 987, <https://doi.org/https://doi.org/10.1029/94JD00911>, 1994.
- 725 Galperin, B., Sukoriansky, S., and Anderson, P. S.: On the critical Richardson number in stably stratified turbulence, *Atmospheric Science Letters*, 8, 65–69, <https://doi.org/https://doi.org/10.1002/asl.153>, 2007.
- Gavrilov, N. M., Luce, H., Crochet, M., Dalaudier, F., and Fukao, S.: Turbulence parameter estimations from high-resolution balloon temperature measurements of the MUTSI-2000 campaign, *Annales Geophysicae*, 23, 2401–2413, <https://doi.org/10.5194/angeo-23-2401-2005>, 2005.

- 730 Gonzalo, J., Lopez, D., Domínguez Fernández, D., García, A., and Escapa, A.: On the capabilities and limitations of high altitude pseudo-satellites, *Progress in Aerospace Sciences*, <https://doi.org/10.1016/j.paerosci.2018.03.006>, 2018.
- Grimshaw, S. D. and Taylor, J. V.: Fast Settling Millimetre-Scale Five-Hole Probes, vol. Volume 6: Ceramics; Controls, Diagnostics and Instrumentation; Education; Manufacturing Materials and Metallurgy of *Turbo Expo: Power for Land, Sea, and Air*, p. V006T05A014, <https://doi.org/10.1115/GT2016-56628>, 2016.
- 735 Haack, A., Gerding, M., and Lübken, F.-J.: Characteristics of stratospheric turbulent layers measured by LITOS and their relation to the Richardson number, *Journal of Geophysical Research: Atmospheres*, 119, 10,605–10,618, <https://doi.org/10.1002/2013JD021008>, 2014.
- Hamilton, J., de Boer, G., Doddi, A., and Lawrence, D. A.: The DataHawk2 uncrewed aircraft system for atmospheric research, *Atmospheric Measurement Techniques*, 15, 6789–6806, <https://doi.org/10.5194/amt-15-6789-2022>, 2022.
- Hasan, Y., Roeser, M., Hepperle, M., Niemann, S., Voß, A., Handoyo, V., and Weiser, C.: Flight mechanical analysis of a solar-powered high-altitude platform, *CEAS Aeronautical Journal*, 14, <https://doi.org/10.1007/s13272-022-00621-2>, 2022.
- 740 Hobbs, S., Dyer, D., Courault, D., Oliosio, A., Lagouarde, J.-P., Kerr, Y., McAnney, J., and Bonnefond, J.: Surface layer profiles of air temperature and humidity measured from unmanned aircraft, *Agronomie*, 22, 635–640, <https://doi.org/10.1051/agro:2002050>, 2002.
- Huang, R., Sun, H., Wu, C., Wang, C., and Lu, B.: Estimating Eddy Dissipation Rate with QAR Flight Big Data, *Applied Sciences*, 9, 5192, <https://doi.org/10.3390/app9235192>, 2019.
- 745 International Met Systems: iMet-XF UAV Sensor Description, <https://www.intermetssystems.com/products/imet-xf-uav-sensor/>, accessed: 2023-08-04.
- Jacob, J. D., Chilson, P. B., Houston, A. L., and Smith, S. W.: Considerations for Atmospheric Measurements with Small Unmanned Aircraft Systems, *Atmosphere*, 9, <https://doi.org/10.3390/atmos9070252>, 2018.
- Kantha, L., Lawrence, D., Luce, H., Hashiguchi, H., Tsuda, T., Wilson, R., Mixa, T., and Yabuki, M.: Shigaraki UAV-Radar Experiment (ShUREX): overview of the campaign with some preliminary results, *Progress in Earth and Planetary Science*, 4, <https://doi.org/10.1186/s40645-017-0133-x>, 2017.
- 750 Kim, S.-H., Chun, H.-Y., Kim, J.-H., Sharman, R. D., and Strahan, M.: Retrieval of eddy dissipation rate from derived equivalent vertical gust included in Aircraft Meteorological Data Relay (AMDAR), *Atmospheric Measurement Techniques*, 13, 1373–1385, <https://doi.org/10.5194/amt-13-1373-2020>, 2020.
- 755 Ko, H.-C., Chun, H.-Y., Wilson, R., and Geller, M. A.: Characteristics of Atmospheric Turbulence Retrieved From High Vertical-Resolution Radiosonde Data in the United States, *Journal of Geophysical Research: Atmospheres*, 124, 7553–7579, <https://doi.org/https://doi.org/10.1029/2019JD030287>, 2019.
- Kolmogorov, A. N.: The local structure of turbulence in incompressible viscous fluid for very large Reynolds numbers, *Dokl. Akad. Nauk SSSR*, 30, 301–305, 1941.
- 760 Lawrence, D. A. and Balsley, B. B.: High-Resolution Atmospheric Sensing of Multiple Atmospheric Variables Using the DataHawk Small Airborne Measurement System, *Journal of Atmospheric and Oceanic Technology*, 30, 2352–2366, <https://doi.org/10.1175/JTECH-D-12-00089.1>, 2013.
- Lenschow, D.: The measurement of air velocity and temperature using the NCAR Buffalo aircraft measuring system, National Center for Atmospheric Research, 1972.
- 765 Liu, X., Xu, J., and Yuan, W.: Diurnal variations of turbulence parameters over the tropical oceanic upper troposphere during SCSMEX, *Science China Technological Sciences*, 57, 351–359, <https://doi.org/10.1007/s11431-013-5445-5>, 2014.

- Luce, H., Kantha, L., Hashiguchi, H., Doddi, A., Lawrence, D., and Yabuki, M.: On the Relationship between the TKE Dissipation Rate and the Temperature Structure Function Parameter in the Convective Boundary Layer, *Journal of the Atmospheric Sciences*, 77, 2311–2326, <https://doi.org/https://doi.org/10.1175/JAS-D-19-0274.1>, 2020.
- 770 NASA: NASA Worldview Snapshots, <https://wvs.earthdata.nasa.gov>, accessed: 2023-07-28.
- Nastrom, G. D. and Gage, K. S.: A Climatology of Atmospheric Wavenumber Spectra of Wind and Temperature Observed by Commercial Aircraft, *Journal of Atmospheric Sciences*, 42, 950 – 960, [https://doi.org/10.1175/1520-0469\(1985\)042<0950:ACOAWS>2.0.CO;2](https://doi.org/10.1175/1520-0469(1985)042<0950:ACOAWS>2.0.CO;2), 1985.
- Rautenberg, A., Graf, M. S., Wildmann, N., Platis, A., and Bange, J.: Reviewing wind measurement approaches for fixed-wing unmanned aircraft, *Atmosphere*, 9, 1–24, <https://doi.org/10.3390/atmos9110422>, 2018.
- 775 Reuder, J., Jonassen, M. O., and Ólafsson, H.: The Small Unmanned Meteorological Observer SUMO: Recent developments and applications of a micro-UAS for atmospheric boundary layer research, *Acta Geophysica*, 60, 1454–1473, <https://doi.org/10.2478/s11600-012-0042-8>, 2012.
- Saddoughi, S. G. and Veeravalli, S. V.: Local isotropy in turbulent boundary layers at high Reynolds number, *J. Fluid Mech.*, 268, 333–372, 1994.
- 780 Sato, T. and Woodman, R. F.: Fine Altitude Resolution Observations of Stratospheric Turbulent Layers by the Arecibo 430 MHz Radar, *Journal of the Atmospheric Sciences*, 39, 2546–2552, [https://doi.org/10.1175/1520-0469\(1982\)039<2546:FAROOS>2.0.CO;2](https://doi.org/10.1175/1520-0469(1982)039<2546:FAROOS>2.0.CO;2), 1982.
- Scoggins, J. R.: Spherical Balloon Wind Sensor Behavior, *Journal of Applied Meteorology and Climatology*, 4, 139 – 145, [https://doi.org/10.1175/1520-0450\(1965\)004<0139:SBWSB>2.0.CO;2](https://doi.org/10.1175/1520-0450(1965)004<0139:SBWSB>2.0.CO;2), 1965.
- Shams, Q. A., Zuckerwar, A. J., Burkett, C. G., Weistroffer, G. R., and Hugo, D. R.: Experimental investigation into infrasonic emissions from atmospheric turbulence, *The Journal of the Acoustical Society of America*, 133, 1269–1280, <https://doi.org/10.1121/1.4776180>, 2013.
- Sharman, R. D., Cornman, L. B., Meymaris, G., Pearson, J., and Farrar, T.: Description and Derived Climatologies of Automated In Situ Eddy-Dissipation-Rate Reports of Atmospheric Turbulence, *Journal of Applied Meteorology and Climatology*, 53, 1416–1432, <https://doi.org/10.1175/JAMC-D-13-0329.1>, 2014.
- 790 Söder, J., Gerding, M., Schneider, A., Dörnbrack, A., Wilms, H., Wagner, J., and Lübken, F.-J.: Evaluation of wake influence on high-resolution balloon-sonde measurements, *Atmospheric Measurement Techniques*, 12, 4191–4210, <https://doi.org/10.5194/amt-12-4191-2019>, 2019.
- Söder, J., Züllicke, C., Gerding, M., and Lübken, F.-J.: High-Resolution Observations of Turbulence Distributions Across Tropopause Folds, *Journal of Geophysical Research: Atmospheres*, 126, <https://doi.org/10.1029/2020JD033857>, 2021.
- 795 Tavoularis, S.: *Measurement in Fluid Mechanics*, Cambridge University Press, 2005.
- Thorpe, S. A. and Deacon, G. E. R.: Turbulence and mixing in a Scottish Loch, *Philosophical Transactions of the Royal Society of London. Series A, Mathematical and Physical Sciences*, 286, 125–181, <https://doi.org/10.1098/rsta.1977.0112>, 1977.
- Treaster, A. L. and Yocum, A. M.: The calibration and application of five-hole probes, Tech. rep., DTIC Document, 1978.
- van den Kroonenberg, A., Martin, T., Buschmann, M., Bange, J., and Vörsmann, P.: Measuring the Wind Vector Using the Autonomous Mini Aerial Vehicle M²AV, *J. Atmos. Oceanic Technol.*, 25, 1969–1982, 2008.
- 800 Van den Kroonenberg, A., Martin, T., Buschmann, M., Bange, J., and Vörsmann, P.: Measuring the wind vector using the autonomous mini aerial vehicle M2AV, *Journal of Atmospheric and Oceanic Technology*, 25, 1969–1982, 2008.
- Wescott, J., SCIENCE, M. U. A. A. I. O., and TECHNOLOGY.: *Acoustic Detection of High - Altitude Turbulence*, Defense Technical Information Center, <https://books.google.com/books?id=pkBFGwAACAAJ>, 1964.

- 805 Whitaker, R. W. and Norris, D. E.: Infrasound Propagation, https://doi.org/10.1007/978-0-387-30441-0_82, 2008.
- Wildmann, N., Hofsäß, M., Weimer, F., Joos, A., and Bange, J.: MASC—a small Remotely Piloted Aircraft (RPA) for wind energy research, *Advances in Science and Research*, 11, 55–61, 2014.
- Williams, P. D. and Joshi, M. M.: Intensification of winter transatlantic aviation turbulence in response to climate change, *Nature Climate Change*, 3, 644–648, <https://doi.org/10.1038/nclimate1866>, 2013.
- 810 Witte, B. M., Singler, R. F., and Bailey, S. C.: Development of an Unmanned Aerial Vehicle for the Measurement of Turbulence in the Atmospheric Boundary Layer, *Atmosphere*, 8, 195, 2017.

Appendix A: Comparison of wind and Reynolds normal stress profiles with and without use of all transducers

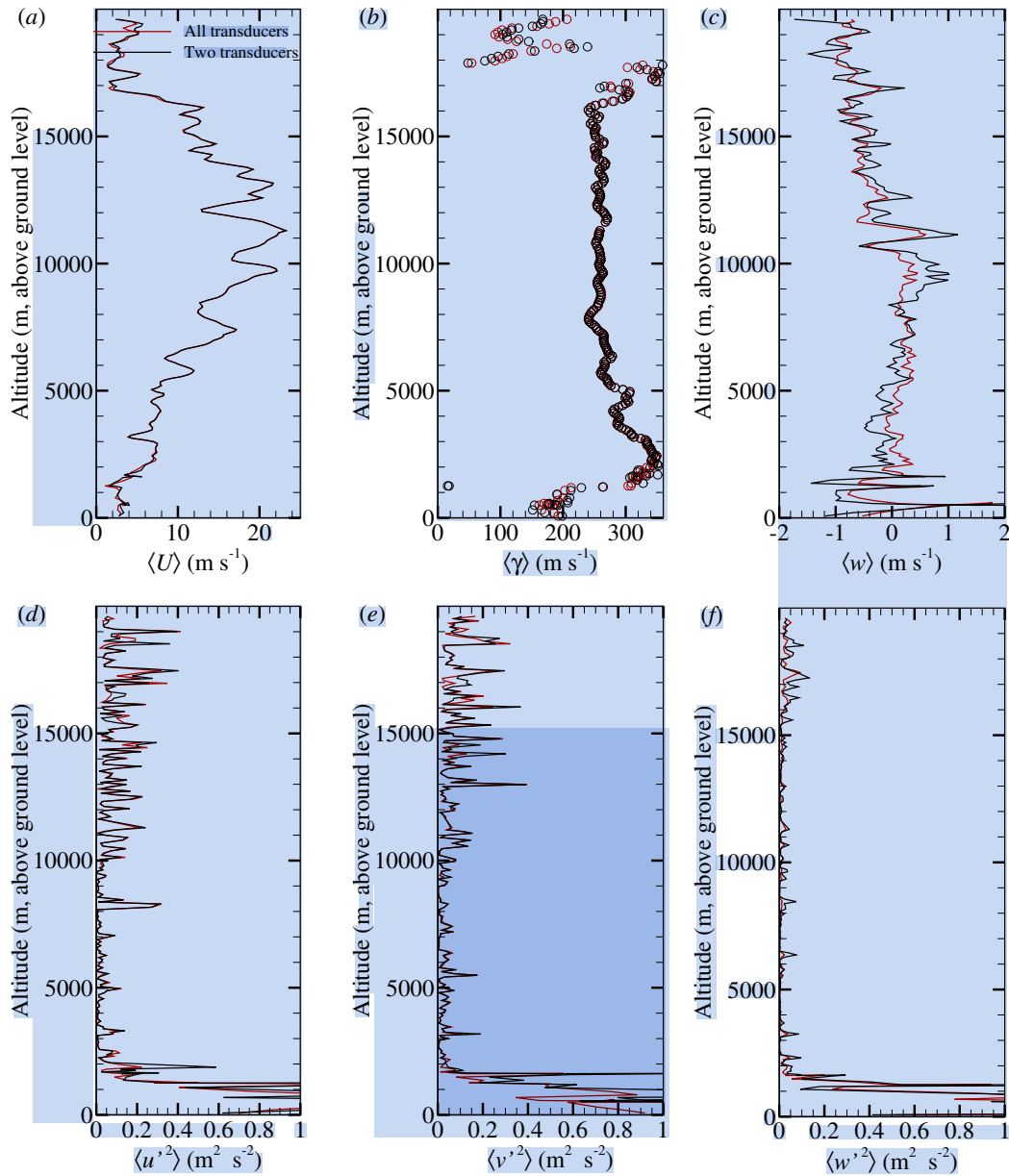


Figure A1. Figures showing comparison of (a) horizontal wind velocity magnitude, (b) horizontal wind direction, and (c) vertical component of wind velocity calculated using all transducers to find Q , α and β and using only two transducers to calculate Q and β with α determined from the aircraft angle of attack measurement. Comparison of resulting (a) $\langle u'^2 \rangle$, (b) $\langle v'^2 \rangle$, and (c) $\langle w'^2 \rangle$ Reynolds stress tensor components.

Appendix B: Upper Air Maps and Satellite Imagery

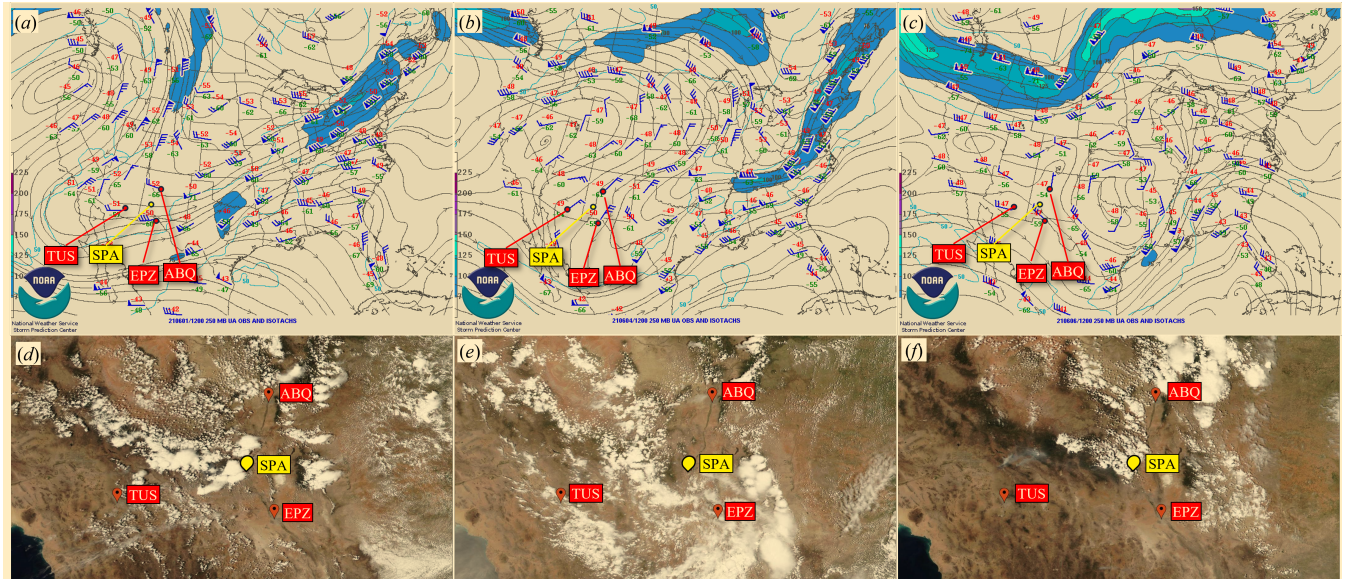


Figure B1. NOAA Jet stream maps at 250 mb (10.366 km) for (a) Flight 1, (b) Flight 2, (c) Flight 3 and satellite images of cloud cover (NASA) for (d) Flight 1, (e) Flight 2, (f) Flight 3. Red pins indicate NWS sounding sites and yellow pin indicates measurement location at SpacePort America (SPA).